Geothermics 121 (2024) 103049

Contents lists available at ScienceDirect

Geothermics

journal homepage: www.elsevier.com/locate/geothermics

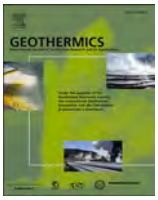

Shallow geothermal field multidisciplinary exploration: New data from Campi Flegrei caldera (CFc) for low—middle enthalpy resource exploitation

Marina Iorio [a,*], Michele Punzo [c], Alberto Carotenuto [b], Giuseppe Cavuoto [c], Alfonso Corniello [d], Vincenzo Di Fiore [c], Giampaolo Donnarumma [a], Maurizio Fedi [e], Nicola Massarotti [b], Nicola Pelosi [c], Daniela Tarallo [c], Maurizio Milano [e]

[a] Institute of Marine Sciences (ISMAR-CNR), Calata Porta di Massa Interno Porto, 80133 Naples, Italy
[b] Department of Engineering, University of Naples 'Parthenope', Naples, Italy
[c] Institute of Heritage Sciences (ISPC-CNR), Via Cardinale Guglielmo Sanfelice 8, Naples, Italy
[d] Department of Civil, Building and Environmental Engineering, University of Studies of Naples 'Federico II", Naples, Italy
[e] Department of Earth, Environment and Resource Sciences, University of Studies of Naples 'Federico II", Naples, Italy

ARTICLE INFO

Keywords:
Multidisciplinary exploration
Geophysics
Hydrochemistry
Low-middle enthalpy exploitation
Volcanic

ABSTRACT

In the framework of the GeoGrid project, with the specific goal to look for shallow geothermal resources suitable to test the developed technologies, the Agnano geothermal field, a relatively unexplored sector of the eastern Campi Flegrei caldera, was investigated through a multidisciplinary geophysical, stratigraphic and hydro-chemical surveys. Such multidisciplinary approach allows us to reconstruct the subsurface morphology below the Agnano Hyppodrome (AH), interpreted by gravimetric, seismic and stratigraphic data, as a complex structure characterized by a gradual southward and south-eastward deepening of a high-density contrast interface. Moreover, the inferred models show two pronounced lateral depressions in agreement with the existence of known lateral faults bounding the western and eastern flanks of AH, while the hydro-chemical survey of the entire Agnano caldera revealed discontinuous manifestations of thermal waters along the groundwater flow direction. Furthermore, it was found that, within the southern sector of the Agnano caldera, mineralized waters predominantly align with a primary NE-SW buried structural lineament, a feature only hypothesized in previous studies and that in this sector local fresh groundwater likely receives endogenous inputs, including CO_2 at elevated temperatures, potentially leading to the mixing of seawater or deep brine. Finally, our results individuate an area north of the Agnano Hippodrome characterized by a significant presence of higher temperature mineralized water, but lacking of seawater enrichment, making it a favorable site for further exploitation of low-to-medium-enthalpy geothermal sources.

1. Introduction

Formation and development of calderas are accompanied by hydrothermal activity, hot fluids circulation and mineralization processes. Deformation and fracturing, produced by both explosive volcanic activity (hydro-magmatic) and collapse resurgence processes, increases the permeability of rocks, enhancing the advection of fluids in the shallow crust and generating a high heat mass transport (e.g., Ingebritsen et al., 2008; Pepe et al., 2019). The Campi Flegrei caldera (CFc) is a large active volcanic complex lying in the Campanian Plain, Southern Italy (Fig. 1). The active volcanic area of CFc has been the site of several geothermal investigations, since the early XX century (Carlino et al., 2016), for its intense hydrothermal activity and thermal properties. Previous studies, in fact, revealed that this area is characterized by temperature higher than 100 °C at the surface, geothermal gradients larger than 200 °C/km, high heat flow, and diffuse magmatic gases discharge at the surface. The thermal energy release, also associated with CO_2 emissions, was estimated in 1998 at about 100 MW (Corrado et al., 1998; Chiodini et al., 2001; Cardellini et al., 2017; Young et al., 2020). A recently empirical evaluation of the geothermal potential of the

* Corresponding author.
E-mail address: marina.iorio@cnr.it (M. Iorio).

https://doi.org/10.1016/j.geothermics.2024.103049
Received 5 January 2024; Received in revised form 11 April 2024; Accepted 2 May 2024
Available online 9 May 2024

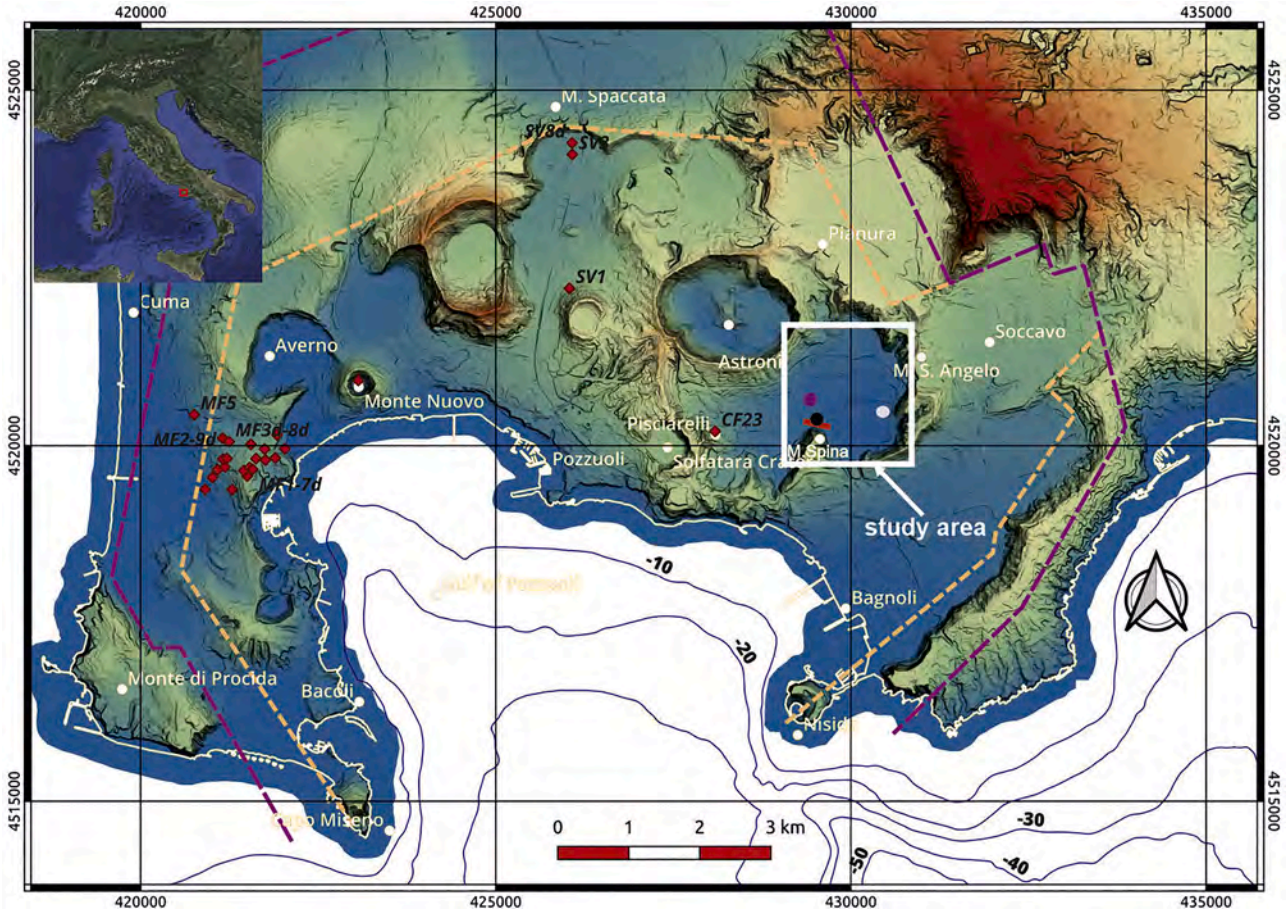

Fig. 1. The CFc caldera rings. Red diamond localization of Agip and ENI geothermal exploration wells in western, northern and central sector of caldera (modified after Carlino et al., 2016). Red line, pink, black and light grey dots in study area: feature active during the Agnano Monte Spina eruptions, vents of epoch 3 (Smith et al., 2011; Orsi 2022 and references therein) and Well 46 localizations (Di Vito et al., 1999), respectively.

whole caldera provided values of few hundreds of MWe (Carlino et al., 2012). However, so far, the geothermal resource at CFc has been used only for spa and wellness, and in very few cases for houses heating. Moreover, the geothermal studies involved mainly geothermal fields, located in western, northern and central sector of caldera (Fig. 1) (Carlino et al., 2016 and reference therein), characterized by very high temperature values at the surface. Only recently low and medium-high enthalpy geothermal systems in the CFc area has been interpreted through a complete western to eastern conceptual models (Siniscalchi et al., 2019; Troiano et al.,2022). These models delineate the presence of two different geothermal reservoirs: one located in the central sector (Solfatara-Pisciarelli zone) dominated by highly active vapors generated by episodic arrival of CO_2 rich magmatic fluids, and the other one located in the eastern sector (Agnano zone), characterized by a shallow (400–500 m b.s.l.) still hot reservoir, heated by the upward circulation of deep no magmatic hot vapor (Siniscalchi et al., 2019; Troiano et al., 2022). The central sector, marked by gas dominance and acidic pH levels, have long been subject of study and extensively monitored, given its proximity to densely populated areas, particularly due to ongoing bradyseism and intense seismic activity (Charlton et al., 2020; Buono et al., 2022; Leone et al., 2022). On the other hand, the eastern sector reservoir is still poorly known in the scientific literature, but its apparent favorable reservoir characteristics (liquid phase and near-neutral pH values) have increased interest in exploring this shallow geothermal field. In the framework of the GeoGrid project (Technologies and Innovative system for sustainability use of geothermal energy, POR Campania FESR 2014–2020) with the main goal to find shallow geothermal resources suitable to test the developed technologies, the physiochemical features of the Agnano aquifers and the surface geothermal reservoir have been determined, for the first time, through a multidisciplinary approach combining gravity, seismic, geoelectric, hydrochemical and groundwater data (Fig. 2). The integration of our results with previously published subsurface geological data provides key information for a better understanding of the structural arrangement and thermal fluid pathways of the Agnano geothermal reservoir. Finally, these results can be used for sustainability analysis of low- and medium-enthalpy resource exploitation, such as for district heating and building cooling (Carotenuto et al., 2016; Iorio et al., 2020) and for assessing the economic feasibility of geothermal exploitation and the development of future project facilities (Calise et al., 2018; Di Fraia et al., 2019; Sepede et al., 2022).

2. Geological and geothermal settings

The CFc volcanic complex hosted in the metropolitan area of Naples, Southern Italy, is constituted by two concentric segmented caldera rings (Tramelli et al., 2006; Acocella, 2010) (Fig. 1) and is characterized by graben-like structures and volcanic deposits, mainly due to the eruptions of the Campania Ignimbrite (CI) (about 40 ky, e.g., Costa et al., 2012; Gebauer et al., 2014; Giaccio et al., 2008, 2017; Scarpati et al., 2013, 2020; Silleni et al., 2020) of the Masseria del Monte Tuff (29.3 ky, Albert et al., 2019) and of the Neapolitan Yellow Tuff (NYT) (about 15 ky Orsi et al., 1992; Scarpati et al., 1993; Deino et al., 2004). Plio-Quaternary continental and marine sediments filled the caldera with a thickness ranging from 2000 to 3000 m. The present morphological depression of the CFc primarily derives from the younger NYT caldera collapse,

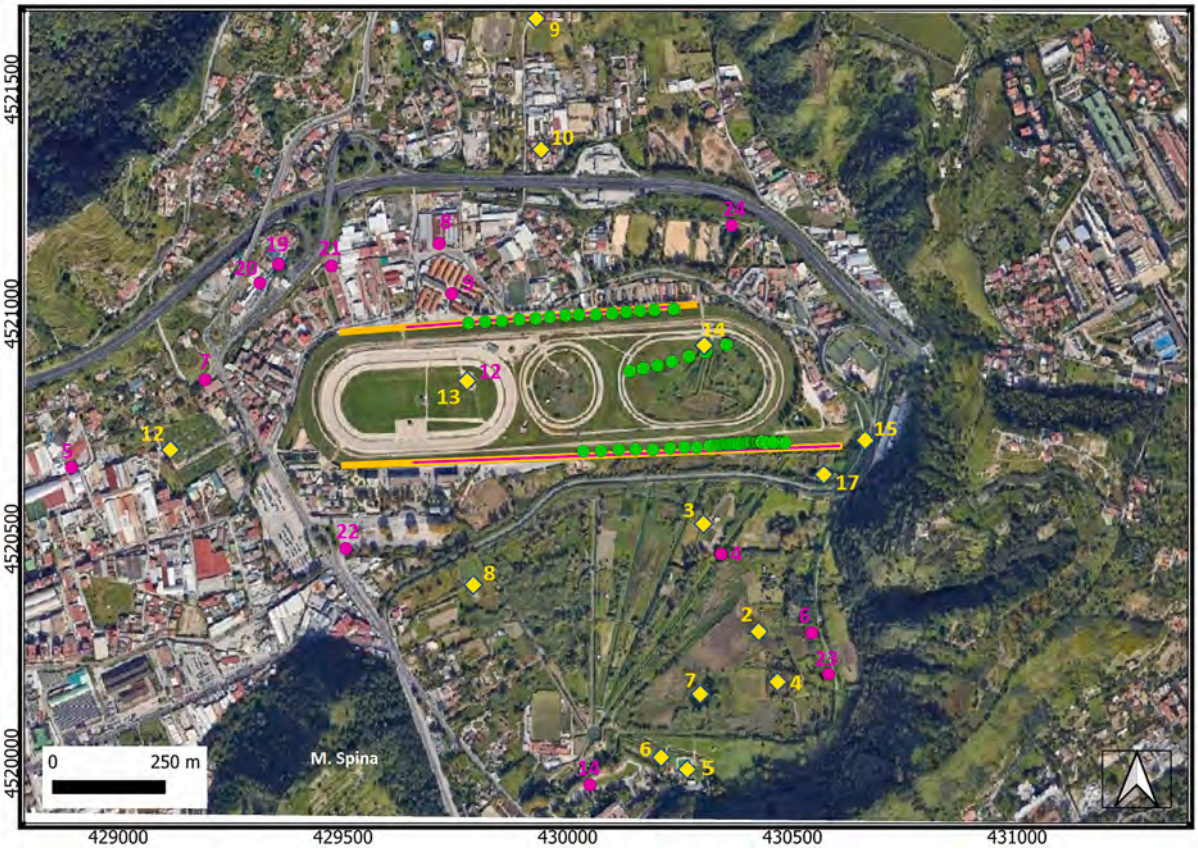

Fig. 2. Localization of all acquired data on orthophoto image (from Google Earth) of the eastern Agnano caldera. Gravimetric (Orange lines), geoelectric (Red lines), and seismic (green dots) profiles along the southern and northern sides of AH. Yellow diamonds and pink circles are the wells sampled for physico-chemical and stratigraphic analysis, respectively. Yellow diamond n°5 is the De Pisis spring.

partially masking the preexisting CF caldera (Orsi et al., 1996; Orsi 2022 and reference therein). After a long period of subsidence, today, the CFc shows signs of potential reactivation, characterized by episodes of ground uplift, shallow seismicity, significant increase in hydrothermal degassing and changes in fluid-geochemistry. Since 1950 several bradyseismic crises occurred, the main of which in the 1982–1984, producing a ground uplift of 1.8 m (D'Auria et al., 2011). After that, a ground subsidence started lasting until 2005, when a new inflation begun, resulting in a minor accelerating uplift (0.4 m over 10 years) of longer duration (Chiodini et al., 2015, 2016). The seismicity recorded since 2000 is very shallow and highly concentrated below the Solfatara crater (e.g., Tramelli et al., 2021, 2022). In the area of renewed seismic activity, the phreatic Pisciarelli field showed the opening of new vents and a significant increase of flow rates and temperatures of existing fumaroles (Chiodini et al., 2015, 2016; Castaldo et al., 2019). Today the amount of the diffusively released of CO_2 (up to 3000 t/d, Cardellini et al., 2017) is that of a persistently degassing active volcanoes. However, moving eastward, the hydrothermal activity in the center of the Agnano crater, e.g. Terme di Agnano, is different to those in the Solfatara-Pisciarelli district, as it consists mostly in the discharge of thermal waters rather than gas (Vaselli et al., 2011; Siniscalchi et al., 2019). The CFc volcanic activity in the last 15 ky was concentrated inside the NYT caldera and stratigraphic markers, as well-recognizable volcanic units (i.e., Monte S. Angelo, Agnano_Monte Spina, Astroni Tephras), paleo sols and absolute age dating, were used from exposed and cored sequences to build up a chronostratigraphic sequence history. So far, the volcanic activity was subdivided in three epochs: from ~15.0 to 10.5 (I), from ~9.6 to 9.1 (II) and from ~5.5 to 3.8 ky (III), respectively (e.g., Rosi and Sbrana, 1987; Di Vito et al., 1999; Isaia et al., 2004; Orsi et al., 2004; Smith et al., 2011; Bevilacqua et al., 2016, Orsi, 2022) separated by two mature and widely distributed paleo sols. Volcanism was mainly submarine during both I and II epochs, while it was subaerial in the III epoch (Di Vito et al., 1999). Complex pyroclastic sequences and four lava units, produced by mostly explosive monogenetic volcanic activity, are the main characteristic of the about 70 volcanic units recognized trough outcrop and borehole sequences (Di Vito et al., 1999; De Vita et al., 1999; Smith et al., 2011; Ascione et al., 2021). The Agnano plain, located in the northeastern sector of CFc, was generated during the third period of CFc activity, by a volcano-tectonic collapse affecting an area of about 6 km^2, related to the ~ 4400 years BP Agnano–Monte Spina eruption (Di Vito et al., 1999; De Vita et al., 1999; Smith et al., 2011). The collapse was preceded by fracturing of the vent area and occurred through variable episodes of sinking. Both fracturing and sinking episodes resulted in the migration of the vent and influenced the dynamics of the magmatic reservoir. The collapsed area was delimited by NE–SW and NW– SE faults that likely resulted from partial reactivation of old faults. The net vertical displacement during collapse was 35 m. The Agnano plain continued to subside at least until the Astroni eruption occurred at about 3800 years BP, and the actual plain shape takes into account this northwestern volcanic apparatus (De Vita et al., 1999). Main information about the stratigraphic sequence unit present in the subsoil of southern sector of the Agnano plain derive from the interpretation of a borehole (Well 46 in Fig. 1) which show an alternance of deposits attributed to Costa San Domenico, Monte S. Angelo, Agnano-Monte Spina and Astroni tephras intercalated by marine and palustrine sediments (Di Vito et al., 1999).

3. Data and methods

Geophysical methods combined with geology and chemical analysis

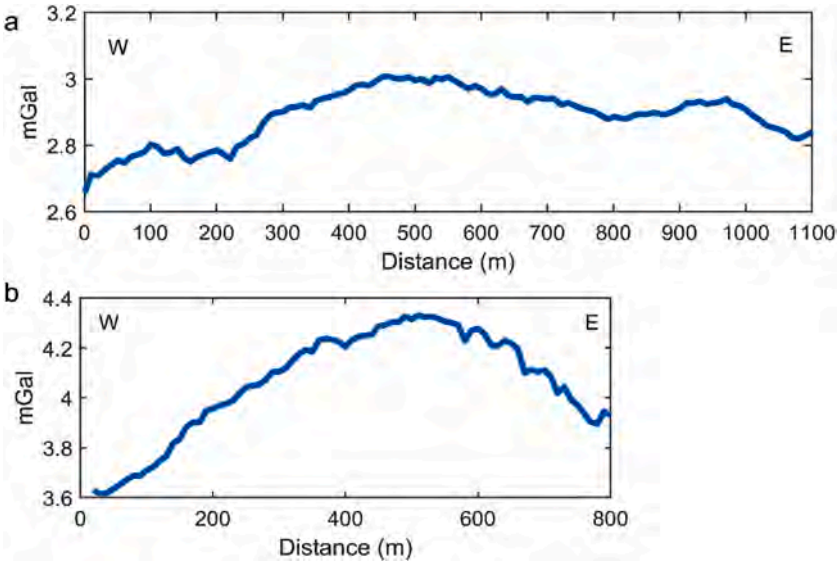

Fig. 3. Bouguer gravity anomalies profiles: a) South; b) North.

of thermal fluids, are very significant for systematic exploration of geothermal reservoirs, due to their permeable characteristics and hot fluids circulations inside conduits such as faults and fractures (e.g., Barone et al., 2019; Muth et al., 2021; Gola et al., 2021). So far, gravity and electrical resistivity surveys represent particularly suitable geophysical methods for the surface exploration of geothermal resources and production fields (Bruno et al., 2007; Carrier et al., 2019; Lichoro et al., 2019). Geoelectric methods, such as electrical resistivity tomography (ERT), have been widely used in geothermal areas, as reservoir temperature, fluid salinity, and hydrothermal alteration cause large variation in the subsurface electrical conductivity or its reciprocal, electrical resistivity (e.g., Ahumada et al., 2022). On the other hand, the gravimetric method can be particularly useful for deriving information about the main lateral density variations, closely associated with subsurface lithological and structural configurations (Telford et al., 1990; Atef et al., 2016; Milano et al., 2020; Guglielmetti and Moscariello, 2021; Varfinezhad et al., 2022).

3.1. ERT survey

The theories and applications of 2D ERT technique to monitor geothermal site (Drahor et al., 2014; De Giorgi and Leucci, 2015; Blázquez et al., 2022) and in general to study the active sector of Campi Flegrei caldera (Gresse et al., 2017; Di Giuseppe and Troiano, 2019), are well established. In this study we conducted two Electrical Resistivity Tomography surveys along the southern and northern sides of AH (Fig. 2). The ERT survey was carried out using an IRIS Syscal-Pro 96-node imaging system with stainless-steel electrodes. The data were collected using the Schlumberger reciprocal array to allow for a high in-depth resolution while maintaining the degree of sensitivity to horizontal changes in resistivity. The two south and north W-E oriented profiles (Fig. 2), were acquired using 96 and 60 electrodes, 10 m equally spaced, for a length of 950 and 590 m, respectively. Electrode coordinates were calculated using a real-time kinematic Global Positioning System (GPS) with 2 cm accuracy. To determine the true subsurface resistivity, an inversion of the measured apparent resistivity values was performed. The datasets were inverted using the software developed by Loke (Loke and Barker, 1996a, 1996b) using a forward modeling subroutine to calculate the apparent resistivity through a nonlinear least-squares optimization technique. The inversion routine is based on the smoothness-constrained least-squares method (Sasaki, 1992), implemented into Occam's optimization algorithm (La Brecque et al., 1996), which contemporary provides the resistivity model and the Root Mean Square (RMS) error between the calculated and the measured pseudo-sections. The interpreted model is, then, considered as a representation of the "true" resistivity of the subsurface, when a close match is made between the modeled resistivity profile and the apparent resistivity inversion profile.

3.2. Gravimetric survey

Two gravimetric surveys were conducted along the two profiles selected for the above ERT surveys, but extending their lengths to 1100 m and 780 m along the south and north sides of AH, respectively (orange lines in Fig. 2). We collected a total of 190 gravity measurements with a 10 m horizontal spacing by using a Scintrex CG-5 AUTOGRAV microgravity-meter, which ensures a 1 μGal (10^{-3} mGal) precision and standard deviation < 5 μGal. The gravimetric dataset was firstly processed to obtain the complete Bouguer anomalies under the usual corrections (e.g., Milsom and Eriksen, 2011). For each gravity station, we estimated the gravity acceleration by averaging three consecutive measurements in order to ensure the accuracy of the measurement below the instrumental standard deviation. The tidal effect was automatically reduced by the CG-5 instrument's built-in software. The drift effect was instead estimated and removed from the data by repeating the measurement at a single base station with a time interval of 1 hour and 30 min. The free-air anomalies were obtained using the classical formula of the free-air reduction $g_{fac} = 0.3086$ h where h is the altimetric distance from the reference ellipsoid. We then obtain the simple Bouguer anomalies using the Bouguer slab formula: $g_{bgc} = 2\pi G\rho T$, where T is the Bouguer slab thickness; $G = 6.67 \times 10^{-11}$ m^3 kg^{-1} s^{-2} is gravitational constant; ρ is the density of the slab (in g/cm^3) (e.g. Milano et al., 2021). We set ρ=2.1 g/cm^3 as suitable density for the shallowest alluvial sedimentary unit of the area. Finally, the terrain correction has been calculated using the Oasis Montaj software and a high resolution DTM, out to 200 km from each gravity station, to obtain the complete Bouguer anomaly using the formula:

$$\Delta g_{cb} = G_o - (G_T + g_{fac}) - (g_{bgc} + g_{tc}) \quad (1)$$

where G_o is the observed gravity; G_T is the theoretical gravity; g_{fac} is the free-air reduction; g_{bgc} is the Bouguer slab correction and g_{tc} is the terrain correction. It should be noted that at the local scale of the microgravimetric survey, the variation of G_T is negligible and can be assumed to be constant. In the following, the gravity anomalies are therefore expressed as relative gravity variations with respect to the minimum

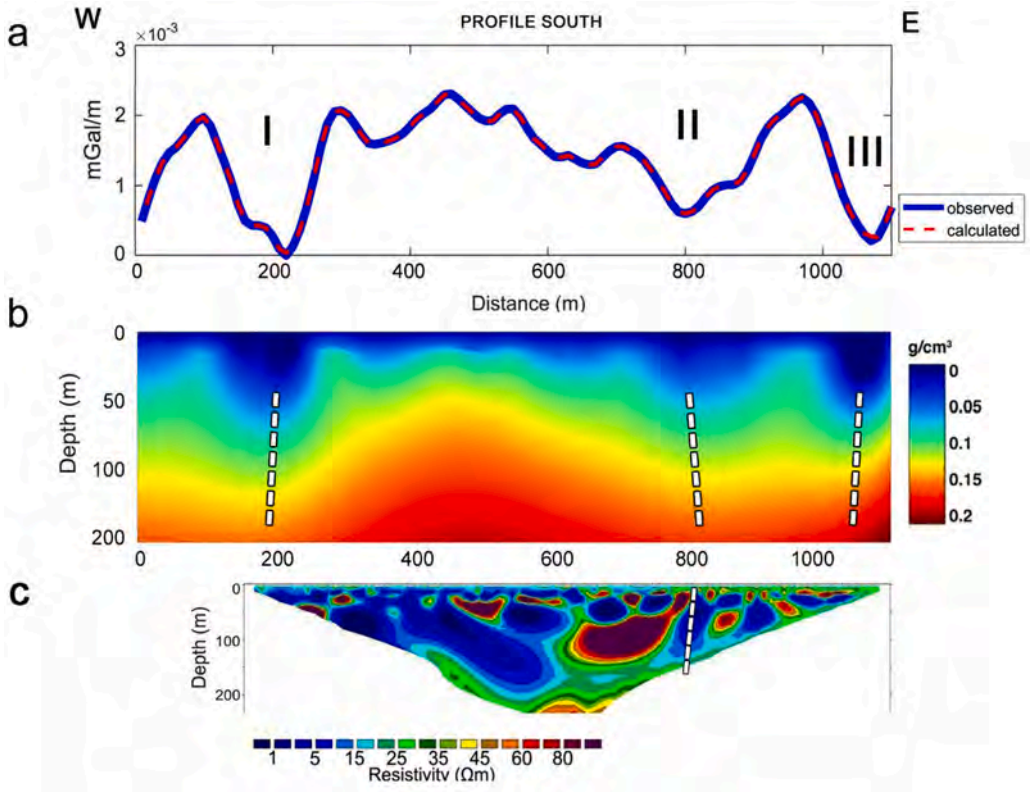

Fig. 4. Results of the CDEXP analysis along profile South. a) gravity data fitting; b) Density contrast model; c) Resistivity model obtained from the inversion of the ERT data. White dashed lines represent the interpreted structural features.

value. In Fig. 3 we show the complete Bouguer gravity anomalies of both southern (a) and northern (b) profiles. The anomalies show a maximum amplitude of about 0.3 mGal along the profile South with three main highs at around 100 m, 500 m and 950 m, while a general higher amplitude is observed in the profile North with a peak at about 500 m.

To investigate the depth, shape and density contrast of the subsurface sources we performed a multiscale analysis of the gravity data by using the CompactDEXP (CDEXP) method (Liu et al., 2020; Baniamerian et al., 2016). The CDEXP is a multiscale iterative imaging method based on the DEXP method (Fedi, 2006). In general, the DEXP transformation of the q^{th} order vertical derivative of the field is defined as (Fedi and Pilkington, 2012):

$$\Omega^{(q)}(x,y,h_i) = h_i^{\left(\frac{q+N}{2}\right)} \frac{\partial^q f(x,y,z)}{\partial z^q}\bigg|_{z=z_i} \qquad i = 1,\ldots,L. \tag{2}$$

where *x, y, z* are the coordinates of the position vector, *f* is the potential field and $h_i=|z_i|$ is the i^{th} depth level that corresponds to the i^{th} altitude. The DEXP method consists of building a 3D dataset by using the upward continuation (e.g., Mastellone et al., 2014) up to the i^{th} altitude. The stability of the upward continuation with respect to high-frequency noise allows applying the DEXP transformation even to high-order derivatives of potential fields (Fedi, 2006). Then, the upward continued field is scaled by a power law whose exponent depends on the source's structural index *N*. The latter is related to the fall-off decay of the field versus distance and reflects the type of source, which for a homogeneous source can be defined as: 0 for contacts, 1 for sheets, 2 for cylinders and 3 for spheres (e.g., Reid et al., 1990). It follows that the correct choice of *N* is crucial for proper imaging of the subsurface sources (e.g., Paoletti et al., 2022). Here we estimated *N* from the gravity data using the technique described in Fedi et al., (2007), Florio and Fedi (2006), and Fedi et al., (2009), which is based on the scaling function analysis of the potential field (see Florio and Fedi, 2006, for details). In particular, the scaling function analysis yields information about the homogeneity degree value (*n*) which is related to the structural index (*N*) by the following formula (e.g., Paoletti et al., 2020):

$$N = -n + q \tag{3}$$

with *q* being the field differentiation order.

The source model provided by the DEXP method, however, consists of a smooth image of the subsurface sources, and the corresponding predicted data may not well fit the measured data. Therefore, such a model can be improved to reconstruct a geologically feasible distribution of the source. This can be achieved by implementing a compacting function, based on the estimated model at the previous iteration (Baniamerian et al., 2016; Liu et al., 2020):

$$\mathbf{W}_i = 1 + \frac{\boldsymbol{\rho}_{i-1}{}^2}{\sigma^2} \tag{4}$$

where $\boldsymbol{\rho}_i$ is the density model obtained at the $(i\text{-}1)^{th}$ iteration, and σ is a positive-value parameter with the same dimension as physical property that controls the degree of compactness or focusing.

Therefore, the model at the i^{th} iteration is given by:

$$\boldsymbol{\rho}_i = \boldsymbol{\rho}_{i-1} + k_i \mathbf{W}_{i-1} \mathbf{A} \boldsymbol{\Omega}_{dif} \tag{5}$$

and accordingly, we obtain the calculated field as:

$$\mathbf{d}_i^{cal} = \mathbf{A}\boldsymbol{\rho}_i \tag{6}$$

where $\mathbf{A}$ is the kernel matrix $\boldsymbol{\Omega}_{dif}$, is the DEXP of data misfit and k_i is a constant. The latter converts the DEXP model into the physical parameter by performing a linear regression of the data misfit vs the field predicted from $\boldsymbol{\Omega}_{dif}$ at the iteration $(i\text{-}1)$ with unit density (Baniamerian et al., 2016).

Therefore, before performing the CDEXP analysis we estimated the

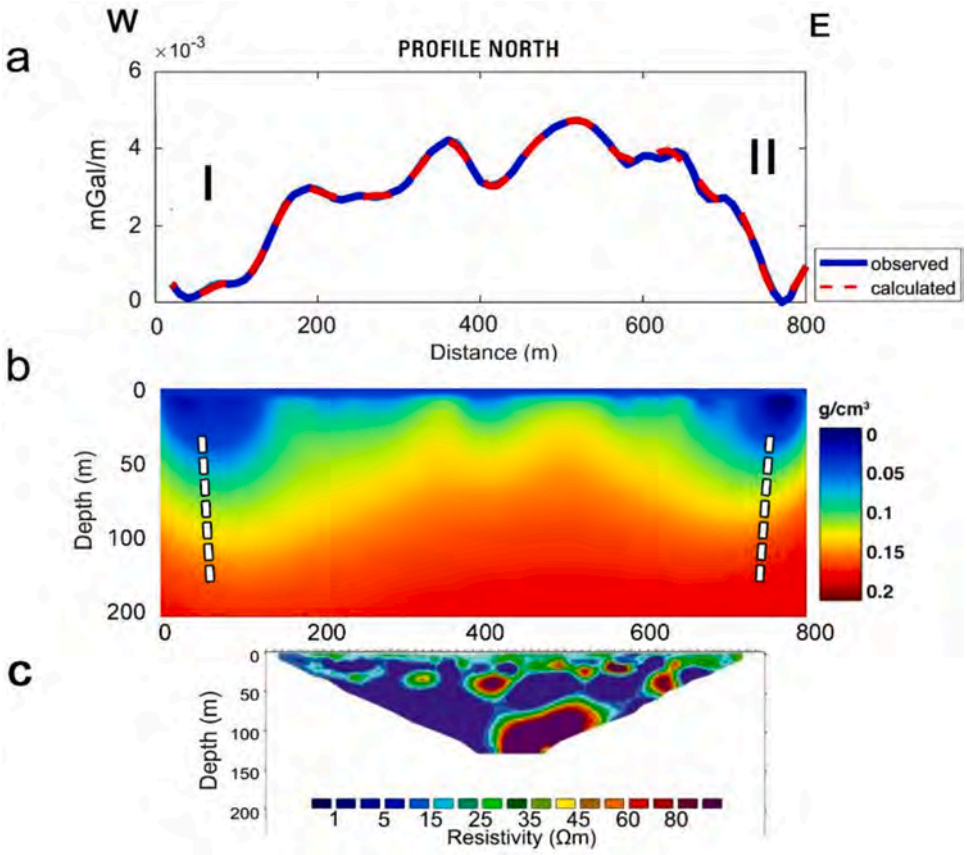

Fig. 5. Results of the CDEXP analysis along profile North. a) gravity data fitting; b) Density contrast model; c) Resistivity model obtained from the inversion of the ERT data. White dashed lines represent the interpreted structural features.

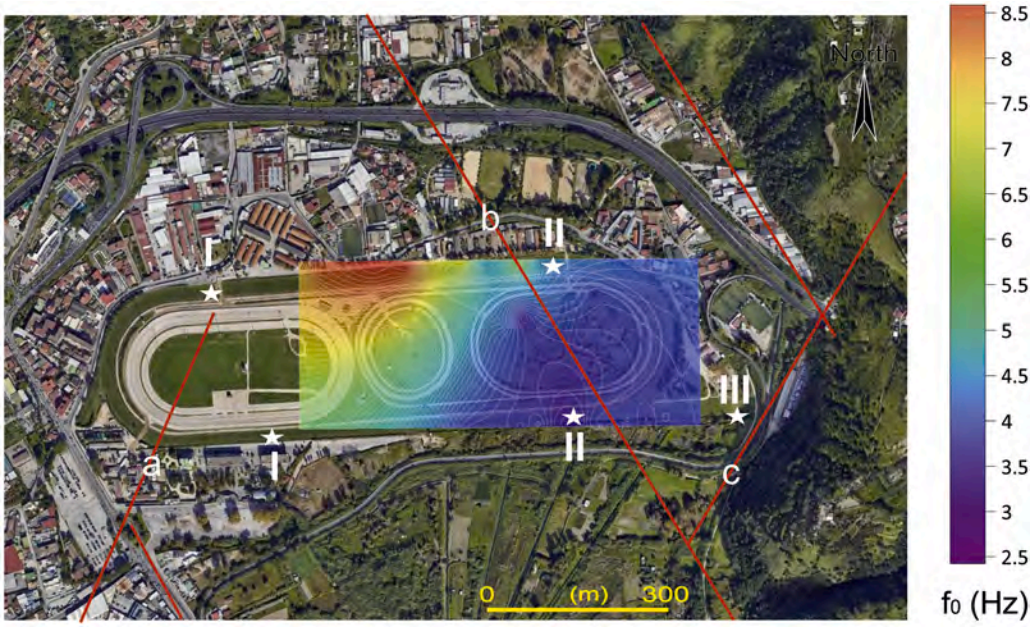

Fig. 6. Orthophoto image (from Google Earth) with superimposition of the contour map of the fundamental frequency peak (f_0) derived from HVSR analysis of microtremor data, gravity anomalies data (I,II,III, this paper) and previously known faults (red lines, after Isaia et al., 2015).

structural index *N* using the scaling function method. However, to better discern the source contributions within the gravity signal, such as density contrasts arising from faults and/or lithological boundaries in the geothermal area, we computed the first-order vertical derivative of the gravity datasets (Kelemework et al., 2021; Sakhare et al., 2023). The scaling function analysis was performed along both profiles, and the results are presented in Supplementary Figure S1. From this analysis, it is evident that by selecting the right depth to the source, the curve of the

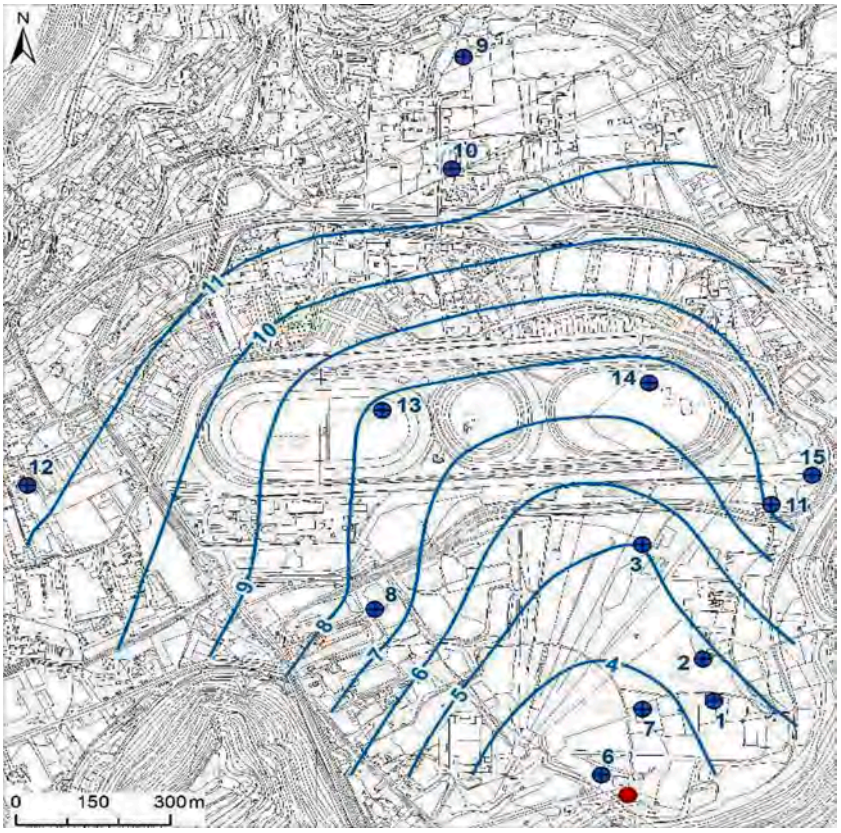

Fig. 7. Groundwater contour lines (in m a.s.l.; June-July 2021). Blue and red dots indicate sampled wells and the De Pisis spring (n° 5 – Table 1) of the Terme di Agnano, respectively.

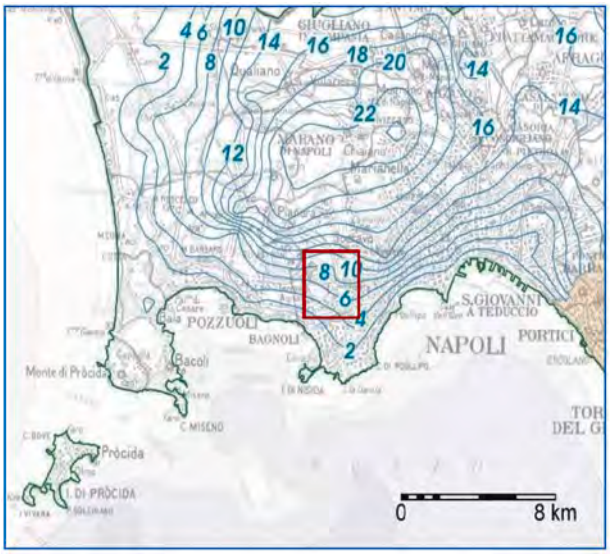

Fig. 8. Study area location (red) and groundwater contour lines (m a.s.l.) of the CFc (from Autorità di Bacino Nord-Occidentale della Campania, 2004).

scaling function becomes flat, with the intercept serving as an estimate of the homogeneity degree, which is approximately $n=-1.1$ for a depth of 0.1 km. Consequently, using Eq. (3) and considering that we employed the first-order vertical derivative of the gravity data ($q = 1$), we derived $N = 0.1$. This value clearly indicates that the causative source of the gravity anomalies along both profiles can be assumed to be very close to the value associated with contact/fault-like sources ($N = 0$) (Reid et al., 1990). In next section we discuss the model inferred from the CDEXP imaging analysis performed for both profiles, to model the main subsurface structures below the AH.

3.3. Seismic noise data analysis

The measurements and analysis of ground vibrations induced by uncontrolled sources, the so-called "environmental seismic noise" (displacements of the order of 10^{-4}–10^{-2} mm) have been carried out along three passive seismic profiles, in the central-eastern sector of the AH, ENE-WSW, WSW-ENE, NE-SW oriented with a length of 455, 455, 210 m, respectively (Fig. 2). Horizontal to Vertical Spectral Ratio (HVSR) measurements of single-station microtremors have been performed with an intergeophonic distances of 35 m and a time sampling of 8 ms. The location of total 35 free-field HVSR measurements, taken on an area of about 0.15 km^2 are shown in Fig. 2. The data were acquired with 4.5 Hz triaxial geophones, all oriented according to a common reference (magnetic north pole). The noise data were amplified and digitized through the use of 24-bit GEODE seismographs and acquired at the sampling frequency of 125 Hz. In order to produce robust estimates of the environmental vibrations field, the overall duration of the recording, for each profile, was over 60 min (SESAME, 2004). The HVSR measurements were acquired in order to evaluate the fundamental frequency f_0 in the study area (Nakamura, 1989; Kramer, 1996), which can be immediately correlated to the period (T) of oscillation of the site ($T = 1/f_0$). The basic goal of HVSR technique is to retrieve information of seismic impedance contrasts in the subsoil, responsible for the seismic resonance phenomena, which supports the creation in very different area of a reference geological model (e.g., Di Stefano et al., 2014; Mulargia and Castellaro, 2016; Imposa et al., 2017; Di Fiore et al., 2020; Nardone et al., 2020; Mitjanas et al., 2021). Geopsy software (Wathelet et al., 2020) has been used to compute the distribution of the natural frequency value; the data were smoothed using the Konno and Ohmachi

Table 1
Physico-chemical data of the 13 water samples wells localized as in Fig. 7; * the analysis of De Pisis spring (n° 5) is from Valentino & Stanzione (2004; analysis of July 1994), see also Venturi et al., 2017; the values in the last column are in meq/L.

no.	Set	T	pH	Cond.	TDS	CO_2	Hard.	Cl	HCO_3	SO_4	Na	K	Ca	Mg	NO_3	As	Fe	Mn	F	Li	Br	Si	$\frac{Ca+Mg}{Na+K}$
		°C		µS/cm	mg/L	mg/L	°F	mg/L	mg/L	mg/L	mg/L	mg/L	mg/L	mg/L	mg/L	µg/L	µg/L	µg/L	mg/L	mg/L	mg/L	mg/L	
1		24,5	6,7	2760,0	1864,0	68,7	43,7	448,0	864,0	191,0	419,0	150,0	118,0	34,6	2,9	0,7	534,2	1610,4	2,8	0,4	1,8	69,8	0,39
2		25,6	6,7	2820,0	1957,0	247,0	44,6	473,0	905,0	160,0	444,0	127,0	133,0	27,6	2,9	32,9	31,4	742,8	3,4	0,3	1,9	84,1	0,39
3		25,1	6,9	2428,0	1567,0	395,0	40,2	363,0	808,0	184,0	385,0	102,0	125,0	21,7	2,9	63,4	282,6	366,1	4,2	0,3	1,6	66,1	0,41
6	A	26,7	6,5	2709,0	1845,0	149,0	41,4	393,0	1194,0	24,1	439,0	126,0	119,0	28,4	< 1	101,2	4030,5	1769,2	1,2	0,3	1,7	59,4	0,36
7		26,5	6,5	2439,0	1548,0	450,0	38,1	285,0	1008,0	183,0	415,0	97,4	109,0	26,5	2,9	19,3	267,1	983,6	4,2	0,4	1,2	86,8	0,36
15		28,5	7,1	2165,0	1520,0	217,0	36,8	354,0	610,0	154,0	317,0	89,0	118,0	17,8	2,4	15,6	39,3	14,0	4,7	0,2	0,7	62,8	0,45
5*		57,0	6,3		7450,0			2910,0	1586,0	282,0	2064,0	257,0	257,0	73,0					1,3			143,0	0,19
9	B	24,4	6,9	1751,0	1185,0	364,0	34,1	140,0	668,0	258,0	260,0	71,2	109,0	16,7	2,1	42,1	1495,8	931,4	5,3	0,2	0,6	72,1	0,51
10		24,5	7,0	938,0	654,0	321,0	21,9	56,9	356,0	69,2	111,0	40,8	70,0	10,6	76,6	41,3	12,1	6,5	3,4	0,1	0,4	64,8	0,73
11		19,5	7,1	1191,0	845,0	279,0	29,4	112,0	274,0	244,0	126,0	71,3	95,3	13,6	< 1	27,4	28,2	438,3	4,7	0,1	0,5	104,0	0,79
12		27,0	7,5	1624,0	996,0	279,0	38,1	147,0	350,0	183,0	151,0	115,0	124,0	17,3	218,0	11,6	11,3	19,6	2,2	0,1	0,4	65,8	0,78
14		22,0	7,2	1263,0	850,0	488,0	28,5	87,3	411,0	210,0	157,0	61,9	91,9	13,4	20,9	51,6	57,1	5,7	4,5	0,1	0,4	58,7	0,66
8	C	27,3	6,7	2360,0	1508,0	664,0	44,2	216,0	1165,0	146,0	422,0	87,6	133,0	26,6	1,8	18,0	295,6	583,3	3,2	0,4	0,8	87.9	0,42
13		39,0	6,9	4129,0	2842,0	487,0	47,6	436,0	2035,0	240,0	874,0	114,0	117,0	44,5	4,4	221,4	1262,3	112,8	1,6	1,2	1,6	85,5	0,23

(1998) method, using a bandwidth coefficient (b) value of 40. Finally, a mean horizontal-to-vertical (H/V) curve was estimated for each point following the standard criteria adopted globally (SESAME, 2004). These parameters define the statistical robustness of the HVSR curve so that the identified curve can be considered significant for the purpose of identifying a possible site resonance frequency. Subsequently, the computed resonance frequency (f_0) is used to estimate unconsolidated sediment thickness and to map the bedrock surface (Ibs-von Seht and Wohlenberg, 1999; Delgado et al., 2000; Parolai et al., 2002). The theoretical bases of this technique are simplified in a 2 layer 1-D model in which parameters are constant within each layer. In the latter case, the depth h of the seismic discontinuity is immediately derived from the free-surface resonance equation:

$$h = V/(4\ f0) \tag{7}$$

where V is the seismic wave velocity of the upper layer and f_0 is the resonance frequency which appears as a peak in the H/V curve (Nakamura, 1989).

3.4. Stratigraphic records

In this study we collected 14 sedimentary records, from wells drilled in the last 50 years in the central-eastern sector of the Agnano caldera, with variables depths ranging from −20 to −107 m, and a new drill performed by the Trivellazioni Italia S.r.L. in November 2017 in the western side of the AH in the frame of GeoGrid project. Their localizations are indicated by pink circles, in Fig. 2. The new well was drilled by means of a small diameter drilling rig and core drilling equipment complete with thermal probes and metrics. The drilling proceeded by core destruction and reached a depth of - 105 m. Its localization is shown in Fig. 2 with number 12.

3.5. Hydrogeochemical analysis

Thirteen water samples and groundwater level measurements (Yellows diamonds in Fig. 2) were collected in twelve pre-existing wells and in the one newly drilled during the GeoGrid project (number 12 in Fig. 2) in the central-eastern sector of the Agnano caldera. Physico-chemical analyses were performed in all the water points collected, and the waters samples chemical data were brought together in homogeneous sets based on the analysis of the Schoeller-Berkaloff diagrams.

3.6. The geogrid viewer: A graphic web application

All collected and geolocalized data have been visualized in the Web Application, Geogrid Viewer, especially developed, through different programming languages (e.g. PHP, HTML 5, CSS), during the GeoGrid project, to allow the integration of all multi-parameter analyzed and interpreted data in an interactive three-dimensional graph format.

4. Results

4.1. Density and resistivity subsurface models

Results obtained from the CDEXP analysis and the ERT data inversion for profiles South and North, are shown in Fig. 4 and 5, respectively. As mentioned above, the CDEXP analysis was performed on the first-order derivative of the gravimetric data, which are shown in Figs. 4a and 5a (blue line) for the north and south profiles, respectively. In particular, along the southern profile (Fig. 4a), the gravity gradient shows two prominent maxima with a wavelength of about 150 m on the western and eastern sides and a broader gravity maximum in the central part. Conversely, three main gravity minima are identified at approximately 200, 800 and 1100 m from W, labelled as 'I', 'II' and 'III', respectively (Fig. 4a). Instead, along the northern profile, we can mainly

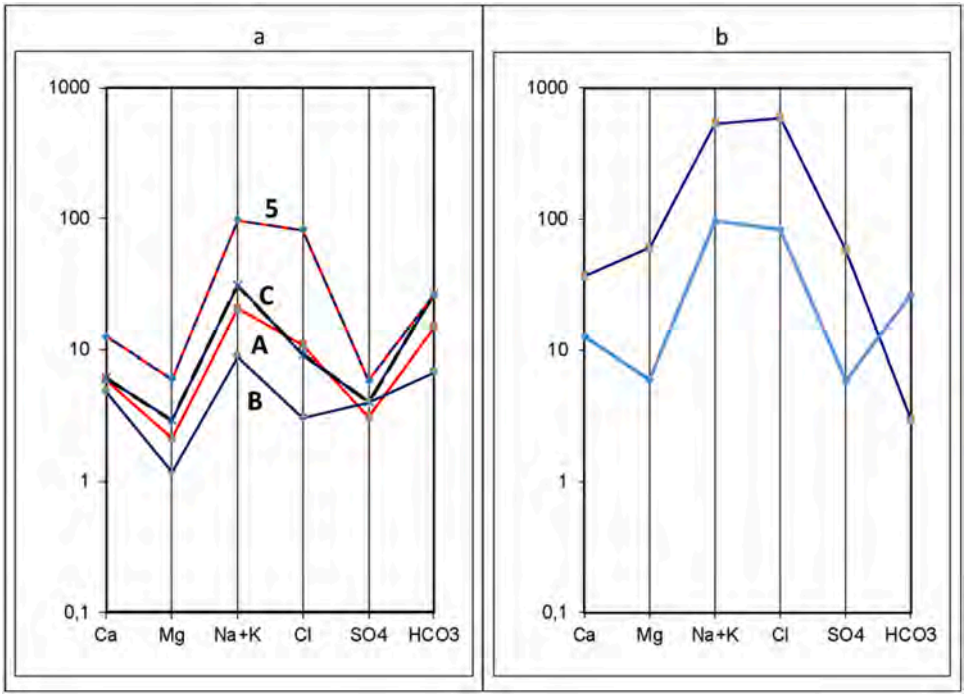

Fig. 9. Schoeller-Berkaloff hydrochemical diagrams (values in meq /L): a) De Pisis spring (n° 5) and mean values of the three water data sets A, B, C (see text); b) seawater (top) and De Pisis spring (bottom) graphs.

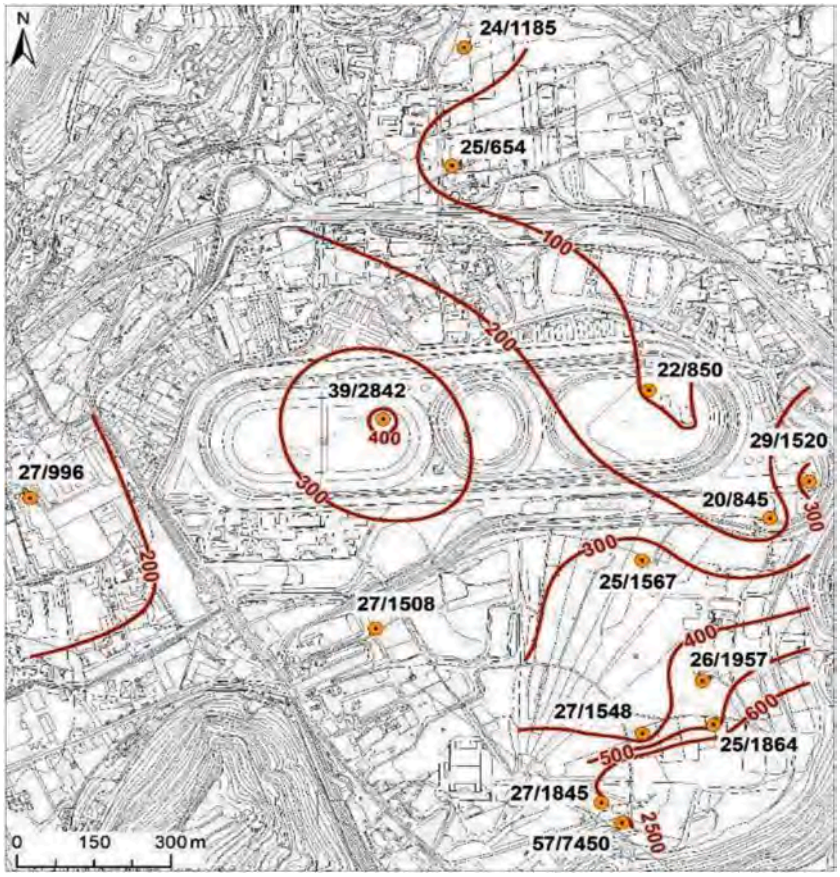

Fig. 10. Cl contour lines (mg/L); numbers close to the wells are respectively T (°C) and TDS (mg/L).

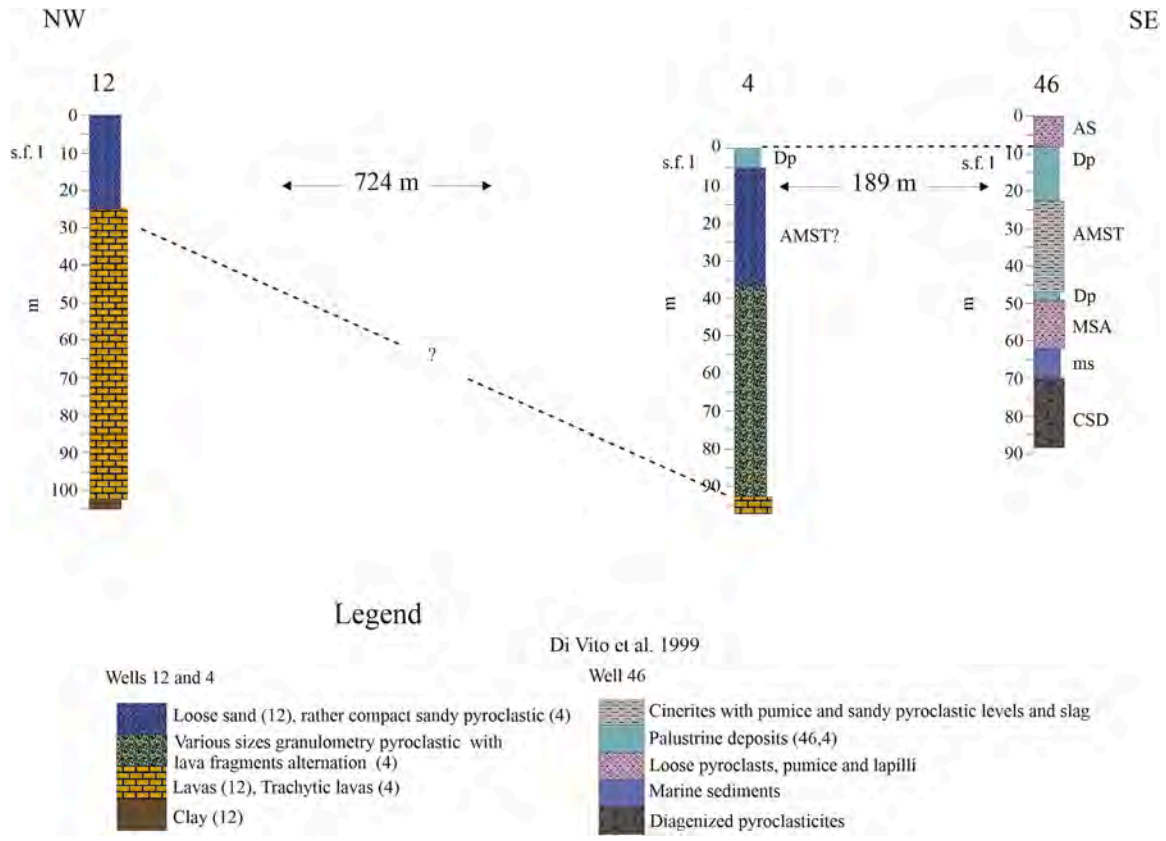

Fig. 11. Stratigraphic logs and hypothesized correlations of wells 12 and 4 (this paper) and well 46 (Di Vito et al., 1999). See Figs. 1 and 2 for localization. Origin of wells 12 and 4: Trivellazioni Italia S.r.L. 2017 (GeoGrid project) and Istituto Nazionale Previdenza Sociale I.N.P.S. (1965), respectively. Sedimentological legend as in Figure. Well 46 stratigraphic position of CFc volcanic units and marine/palustrine deposits: Costa San Domenico tephra (CSD), Monte Sant'Angelo tephra (MSA), Agnano Monte Spina tepra (AMST), Astroni 1,2,3 tephra (AS), as recognized by Di Vito et al. (1999).

identify a gravimetric high in the central part, laterally delimited by two main gravity lows, again labelled as 'I' and 'II' in Fig. 5a. However, in this case, we do not recognize a third eastern gravity low as for profile south, probably due to the limited extension of the northern profile compared to the southern one. Additionally, for both datasets, we also show the data calculated from the derived model at the end of the iterative process (dashed red lines), allowing us to observe a very good fit obtained for both profiles (Fig. 4a and 5a). The inferred CDEXP models in Figs. 4b and 5b show a complex subsurface architecture with density contrasts gradually increasing with depth up to about 0.2 g/cm^3 and probably controlled by structural elements. Along the southern profile (Fig. 4b), the model shows a general trend of high density values at shallow depths (~40 m) bordered by three depression characterized by lower density values (dashed white lines in Fig. 4b), located approximately at 200, 800 and 1100 m from the west. Such a structural setting is consistent with the three gravity lows observed in the gravity gradient ('I', 'II' and 'III' in Fig. 4a) and with the large central gravity maximum ($> 2 \times 10^{-3}$ mGal/m) between 200 and 800 m (Fig. 4a). Furthermore, the near asymmetry of the large central gravity maximum is also reflected in the gravity model, where the higher density layers (0.1–0.2 g/cm^3) show sharp and gradual deepening to the west and to the east, respectively (Fig. 4b).

Similar results are evident along the northern profile shown in Fig. 5b. The model indicates high density values at shallow depths (~20 m) within the central region and the presence of two prominent lateral depressions which align with anomalies 'I' and 'II' identified in the gravity gradient profile (Fig. 5a), situated roughly at 50 and 750 m from west to east, respectively. Moreover, given the parallel alignment of the western starting points of the two gravimetric surveys (Fig. 2), a westward shift of about 150 m of the anomaly 'I' is observed moving from the southern gravity profile to the northern one, while this shift is not observed for anomaly "II". Finally, the easternmost depression of the south profile, associated with gravity minimum 'III' in Fig. 4b cannot be identified along the north profile due to its limited extent. Passing to the ERT data, it is found that the low resistivity values obtained for the two models (1 to 150 Ωm) (Fig. 4c and 5c) are in good agreement with previous 2-D ERT studies carried out in neighboring areas (Bruno et al., 2007; Byrdina et al., 2014; Isaia et al., 2015; Gresse et al., 2017). Moreover, knowing that the resistivity distribution can be interpreted in terms of soil lithology, degree of saturation and that resistivity increases are linked to grain size and cementation, the ERT profiles were compared to the gravimetric surveys. Although the two ERT profiles were limited in extent respect with the gravimetric profiles, we can observe an overall agreement in the geological interpretation of central eastern sector, where resistivity values, reaching up to 80 Ωm could correspond to the presence of non-consolidated pyroclastic and tephra deposits (Gómez-Ortiz et al., 2007; Komori et al., 2014). Moreover, along the sector of southern ERT profile covering the gravity profile, it is possible clearly recognize a structural element at about 800 m corresponding to the anomaly II of the gravimetric profile (Fig. 4b and 4c white dashed line), reaching almost the same depth as observed in the density model. In addition, both resistivity models provide useful information about the subsurface hydrothermal system which is identified by very low values of the electrical resistivity (<20 Ωm) in the western sides of both profiles (Fig. 4c and 5c). In fact, these areas of low values could indicate the presence of structures that favor the rise of hydrothermal fluids, likely associated with structural depression corresponding to the gravity anomaly 'I' (Fig. 4a and 5a), not detected by the ERT profiles because of their limited extension.

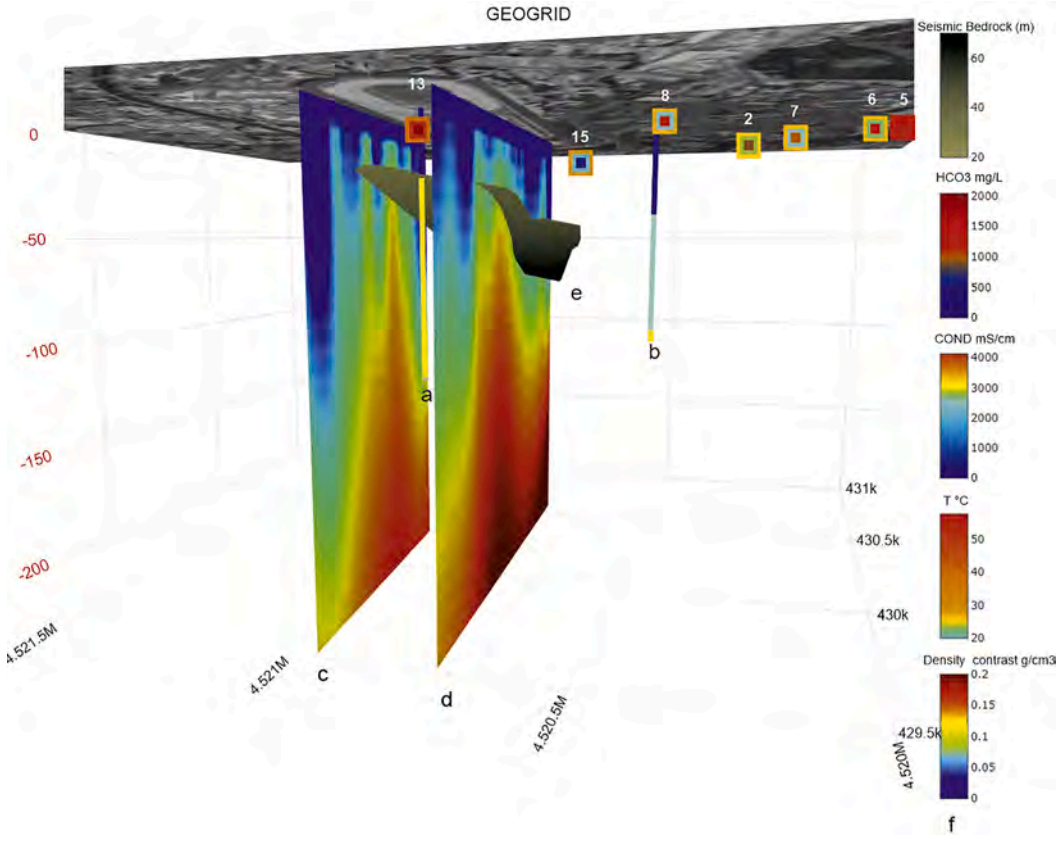

Fig. 12. Geo-localization of gravimetric, seismic, stratigraphic and Physico-chemical data presentation (Geogrid Viewer software). Large, middle and little squares indicate temperature (°C), conductivity (μS/cm) and hydrogen carbonate contents (mg/L) of selected water samples (see text for details) respectively. Columns: a e b wells 12 and 4 stratigraphic logs (see text for color scale meanings), c and d North and South gravimetric profiles, e Seismic bedrock from −25 to −70 m, f data scales.

4.2. Passive seismic model

The HVSR peaks frequencies determined at each point were used to plot the isofrequency contour, showing the f_0 of the overburden (Fig. 6) associated with the thickness of the surface layers above the seismic bedrock (Molnar et al., 2022). Microtremor measurements provided a frequency range from 2.42 to 8.58 Hz for the fundamental resonances of sites. Subsequently the principal seismic impedance contrasts recorded in the 35 site tests were translated in stratigraphic information using the Eq. (7) and an average V_S value equal to 650 m/s (Petrosino et al., 2006). The Eq. (7) leads to detect an impedance contrast from about −20 to −70 m depths from the northcentral to southeastern sector of AH. These depth changes suggest a southeastward deepening of the seismic bedrock surface and an increase in the thickness of the sedimentary cover. Such bedrock trend does not appear to be related to known faults (Fig. 6). However, it is also not possible to attribute the observed undulations in the bedrock to an unknown structural element oriented in the NE-SW direction (e.g., a structure connecting anomalies II and I of the northern and southern gravimetric profile of AH, Fig. 6), either because of the presence in the southern gravimetric profile of a central maximum showing a gradual deepening toward the east (Fig. 4a, b), or because of the uncertainty on the interpolated seismic data, due to the limited coverage, in the south-central sector of AH (Fig. 2).

4.3. Hydrogeological data results

The groundwater level survey in thirteen wells in the east-central sector of the Agnano caldera (Fig. 7) shows, even locally, the presence of a single groundwater body due to the concordance of water levels in wells of different depths. These levels are in agreement with previous data which indicate that, in the CFc, meteoric waters feed a single groundwater body with the highest level (22 m a.s.l.) recorded in the Marano-Calvizzano area and with a radial runoff reaching the sea along the coastline. Elsewhere, groundwater determines subsurface flows to the plains bordering the Campi Flegrei area (Corniello and Nicotera, 1981; Autorità di Bacino Nord-Occidentale della Campania, 2004; De Vita et al., 2018) (Fig. 8). Moreover, the groundwater contour lines in Fig. 7 show a sharp drop due to the drainage exerted on the groundwater by the Agnano caldera outlet channel. In the south-eastern area of the Agnano caldera, De Pisis spring (Fig. 7), which is thermal ($T > 50$ °C) and rich in CO_2, determines anomalous groundwater levels around the spring. Specifically, the groundwater level is approximately 7 m above sea level in an area where groundwater levels are typically lower (see also Bruno et al., 2007).

4.4. Geochemical data results

Physico-chemical analyses were performed in all water points in Fig. 7. The results are shown in Table 1, in which the waters, based on the analysis of the Schoeller-Berkaloff diagrams, were brought together in three homogeneous data sets (A, B, C). Moreover, we observe that arsenic values in groundwater are above the potability limits throughout the area (10 μg /L – Italian Legislative Decree 18/2023).

Set A: includes water samples n° 1, 2, 3, 6, 7 and 15 of the eastern sector of the Agnano caldera (Fig. 7 and Fig. 9a); these waters have high salinity (average TDS = 1718 mg/L) and an average value of [(Ca + Mg)/(Na + *K*)] = 0.39 (values in meq/L, here and elsewhere). Similar water characteristics are shown by the De Pisis spring (Fig. 7 and n°5 in Fig. 9a) which has: $T = 57$ °C; TDS = 7450 mg/L and [(Ca + Mg)/(Na + *K*)] = 0.19. The chemical characteristics of the spring and Set A water samples are influenced by their proximity to the faults system (Di Vito et al., 1999; Isaia et al., 2015). It is likely that high temperature gases

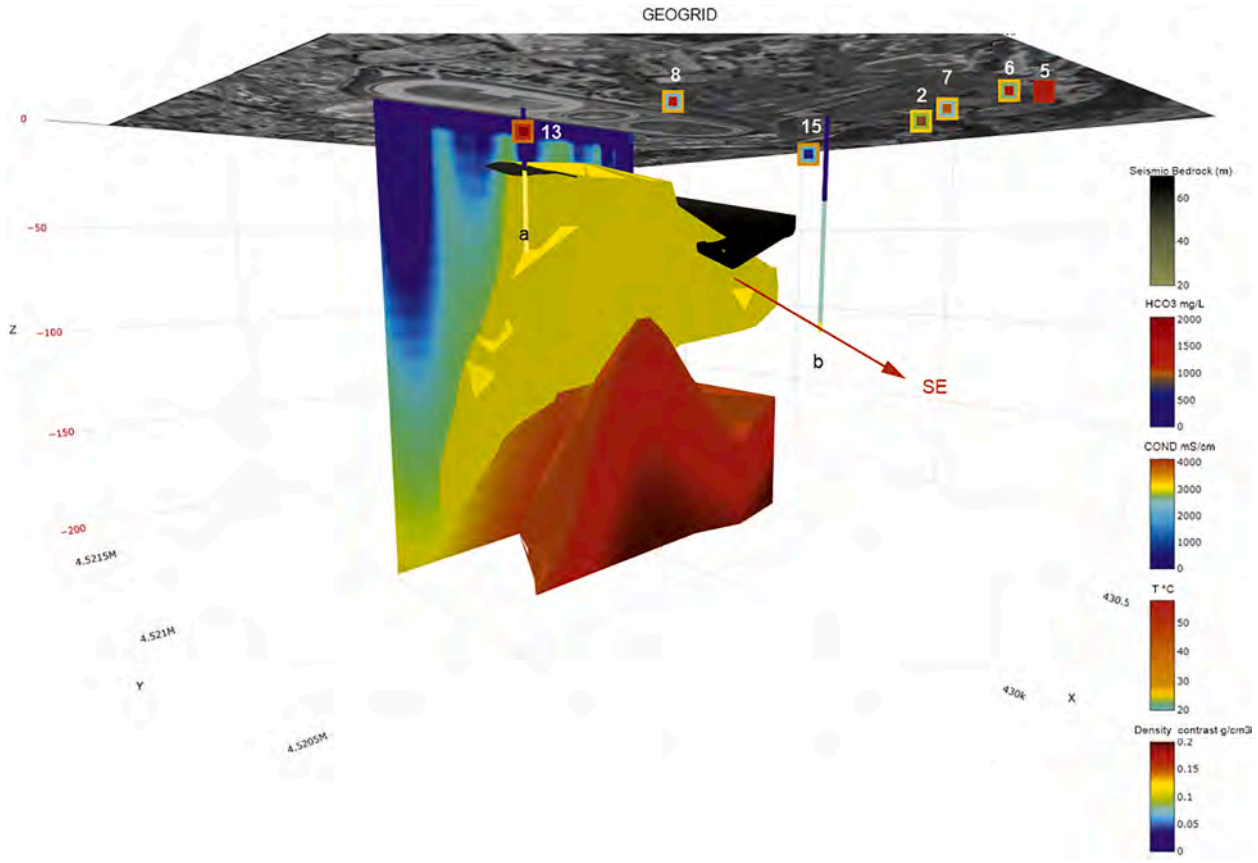

Fig. 13. South-western view of the 3D subsoil morphology of Eastern Agnano caldera by gravimetric (intervals 0.10–0.12 and 0.16–0.2 g/cm^3), seismic, stratigraphic and Physico-chemical data. Red arrow indicates the south-eastward deepening of the seismic bedrock and of the density model. Meanings of large, middle, little squares and columns a and b as Fig. 12.

(essentially CO_2) rise along the faults increasing the reactivity of the groundwater towards the reservoir rock. The rising would be particularly intense at the De Pisis spring and less significant for the other waters of the set; in addition, the chemical profile of the De Pisis spring tends to the typical profile of seawater (Fig. 9b).

In fact, given the proximity of the Agnano caldera to the sea, the upward movement of deep-seated gases is likely to introduce seawater or deeper brine into freshwater sources (Valentino and Stanzione, 2004; Ebrahimi et al., 2022). This phenomenon is particularly pronounced at the De Pisis spring (n° 5) and to a lesser extent in surrounding areas (see Fig. 10). The composition of the infiltrating fluid may indeed include brine, indicated by a Br/Cl ratio exceeding that typically found in Mediterranean waters ($\sim 3.4 \times 10^{-3}$, Yongje et al., 2003; Yasong et al., 2021), especially considering the limited human activity in the vicinity, which would rule out an anthropogenic source of bromine (Adel et al., 2012). Moreover, the elevated HCO_3 concentration in the De Pisis water sample (n° 5) compared to seawater is attributed to its high CO_2 content.

Set B: includes the water samples in the northwestern area of the caldera (n° 9, 10, 11, 12 and 14 in Fig. 7 and Fig. 9a). Here the average TDS is 906 mg/L and the average value of the ratio ionic [(Ca + Mg)/(Na + *K*)] is 0.69. This chemism (Fig. 9a) is consistent with that of the common waters of the CFc (Corniello, 2009).

Set C: includes the water samples of wells n° 8 and 13 (Fig. 7 and Fig. 9a) which have a chemical graph similar to the water samples of data set A but showing higher thermal levels and CO_2 content, with the exception of the De Pisis spring (Fig. 10).

4.5. Stratigraphic data correlations

Among the fourteen sedimentary well records analyzed (Fig. 2), only those belonging to wells 4 and 12 were considered useful to interpret the geophysical models. The stratigraphy of well 12 (this paper, 105 m of recovery) consists, from top to bottom, of 25 m of loose sand, 78 m of lavas deposits, and 2 m of clay sediments (Fig. 11). In well 4 (drilled by Istituto Nazionale Previdenza Sociale, I.N.P.S), however, the upper 5 m consists of marsh deposits, followed below by 32 m of rather compact sandy pyroclastic deposits, between −37 and −93 m, an alternation of different sizes pyroclastic deposits with lava fragments is found, while trachytic lavas are recovered from −93 to −98 m (Fig. 11).

So far, the most interesting characteristic for both wells 12 and 4 is the presence of lavas deposits at different depths (−25 and −98 m, respectively). Even though it is not possible to attribute a certain origin to the recovered lava deposits based only on sedimentary descriptions, however the recovered lavas could probably belong to the Agnano-Monte Spina eruption due to the position of well 12. In fact, well 12 is close to the northern side of Monte Spina hill (Figs. 1 and 2) where Di Vito et al. (1999) reports the presence of not exposed Monte Spina lavas. In addition, Orsi (2022) (and reference therein) always in the same area, indicates the presence of a structural feature active during the Agnano Monte Spina eruption and vents active in epoch 3 (Fig. 1). Nevertheless, the affiliation of these deposits with nearby eruptions of the Astroni volcano cannot be totally excluded, as Tonarini et al., (2009), report that two out of seven eruptive events ended in low-energy explosions and lava extrusion.

The proximity of well 4 to well 46 (Fig. 2), for which volcanic units and marine/palustrine deposits are well-related to CFc eruptions (Di Vito et al., 1999), allows a potential correlations. However, as shown in Fig. 11, this correlation is feasible for the uppermost palustrine deposits alone. Given that these deposits lie beneath the Astroni deposits, it is plausible to propose a connection between the recovered lava deposits in

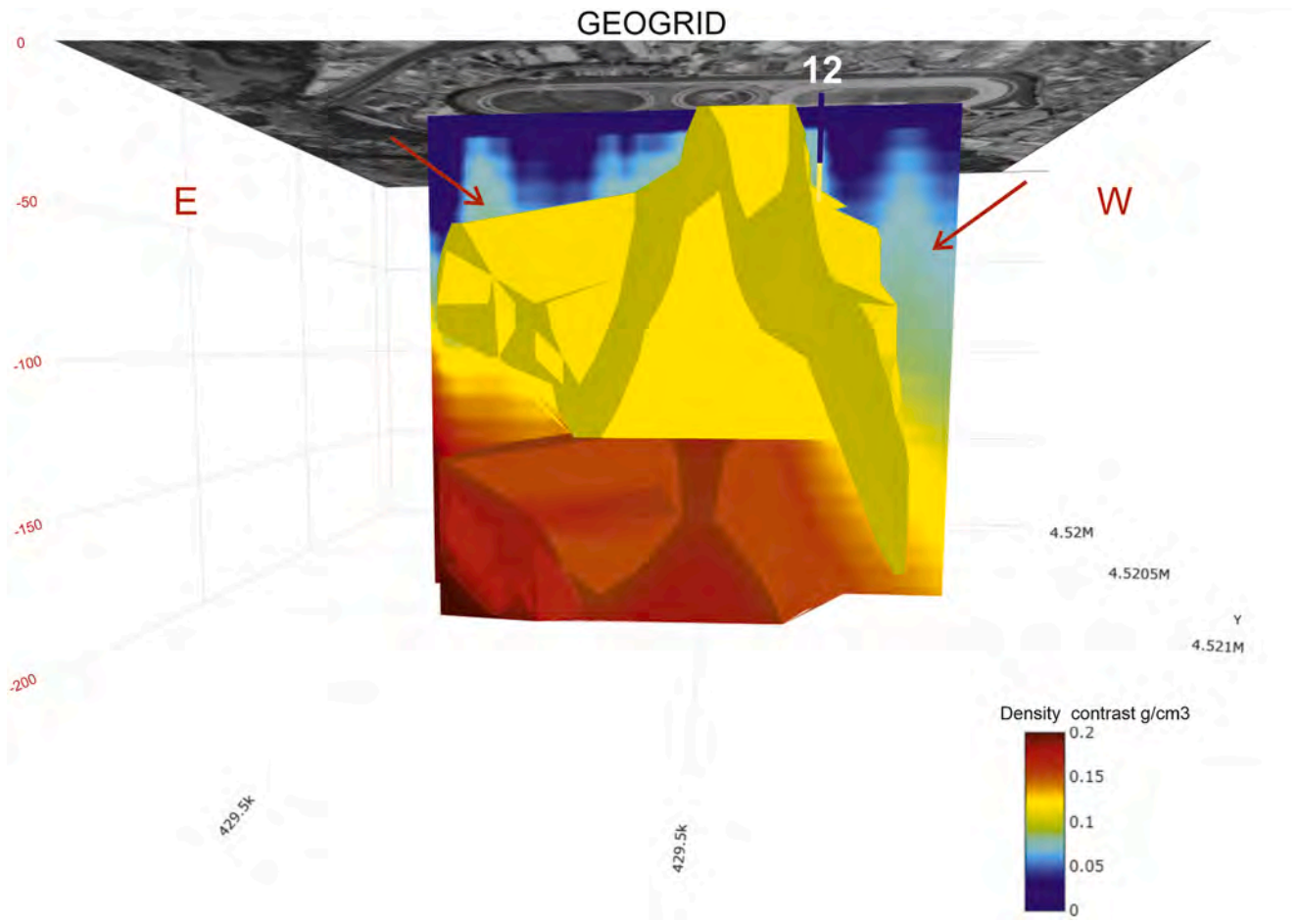

Fig. 14. Northern view of the 3D subsurface morphology model of Agnano caldera. The density contrast models (intervals 0.10–0.12 and 0.16–0.2 g /cm^3) identify a western and eastern subsurface morphology variability (Red arrows). Data scale as legend. Well 12 (number12) stratigraphic logs (see text for color scale meanings).

well 4 and the Agnano Monte Spina volcanic event, rather than the Astroni event.

The different recovery depths of the lava deposits in wells 12 and 4 (Fig. 11) are strictly in agreement with the deepening of the seismic bedrock (e in Fig. 12), allowing us to assume the probable existence of a single lava body displaced during the volcano-tectonic collapse of the Agnano plain. This hypothesis is consistent with de Vita et al., 1999, who calculated, based on the volcanic units of well 46, a net lowering of the plain of 60 m following multiple phases of fracture and collapse. If we subtract this 60 meter from the lava depth (−93 m) of well 4, the lava deposits will reach approximately a depth of −30 m, so a depth similar to that of the lavas (−25 m) observed in well 12. The presence of a single lava body, if confirmed, would suggest a non-uniform sinking of the Agnano plain.

5. 3D model of north Agnano caldera and discussion

Here we provide a multidisciplinary 3D representation of the AH subsurface by integrating the gravimetric and seismic modeling results, the wells stratigraphy data (12 and 4) and 7 on 14 water samples of which temperature, conductivity and hydrogen carbonate (T, Cond and HCO_3 respectively in Table 1) values are > of 25.5 °C, 2000 μS/cm, 600 mg/L (Fig. 12).

It is worth noting that the two gravimetric models show similar density contrast values at different depths, which also agree with the main lithological boundaries deduced from both wells 12 and 4 (Fig. 12a, b, c and d). In particular, the shallowest sector, down to about −40 m, has low density values (0–0.06 g/cm^3), which are interpreted, based on the stratigraphy of wells 12 and 4, as marsh and loose sandy pyroclastic deposits (Blue-light blue colors in both gravimetric models and wells of Fig. 12). At greater depths, on the south-eastern side of AH, we observe a close correspondence between the density contrast values (0.07 to 0.09 g/cm^3) and the sedimentary unit of well 4 down to −93 m, associated with pyroclastic and lava fragments deposits of different sizes (Heavenly-light green colors in both gravimetric models and well 4 of Fig. 12c, d and b). Finally, we observe the higher density contrast values (0.10 up to 0.2 g/cm^3) (Yellow to deep red colors in Figs. 12c and d) interpreted as corresponding to the lavas deposits found in wells 12 and 4 at depths ranging from −25 to −103 m and from −93 to −98 m, respectively. (Yellow color in Fig. 12a and b). From the linear interpolation, through a grid of 70-meter intervals, of the wells stratigraphy and density contrast models, 3 additional profiles were generated from the Geogrid viewer software (at 70, 140 and 210 m from the AH southern gravity profile towards the northern one). The additional profiles were generated assuming that, due to the short distance (~300 m) between the two gravity profiles, the gravity model depressions relative to anomalies I and II are corresponding to same geological structures crossing both profiles. Subsequently, within the Geogrid viewer software, density contrast values, from both the obtained and generated profiles, were clustered in several data sets. The data set intervals were chosen based on the main sedimentological well characteristics. Finally, we used the Delaunay triangulation method (Delaunay, 1934) to develop a 3D model of the lithological/density contrast data sets beneath the AH. In Fig. 13, among the available dataset, the 3D models relative to intervals 0.10 to 0.12 g/cm^3 (Yellow) and 0.16 to 0.2 g/cm^3 (Red) are shown.

Fig. 15. Orthophoto image (from Google Earth) with superimposition of previously known faults (Red Lines) after Isaia et al., (2015). White stars and labels for gravimetric anomalies I, II and III for both north and south profile. Squares, circle and numbers for wells sampled for Physico-chemical and stratigraphic analysis meanings as Fig. 12. White dot hot spring today hidden by highway foundations (Data from Plans for agricultural land Società Napoletana per le Terme di Agnano). White dashed line for alignments of water samples with $T >$ of 25.5 °C, Cond > 2000 μS/cm and HCO_3 values comprise from 600 to 1600 mg/l.

From the models it is possible to notice a subsurface morphology with a general south-eastward decreasing and this finding is in agreement with the deepening trend of the bedrock surface (e in Fig. 12) obtained by the passive seismic data. Subsequently the seismic bedrock surface was incorporated in the 3D model, confirming in particular: the presence of lava deposits at −25 mt in well 12 (a in Fig. 13), the high density layers shallow trend (~20 m) for the north gravimetric model (Fig. 5b) and the eastern gradual deepening for the south gravimetric model (Fig. 4b). Finally the subsoil morphology variability in the 3D model is shown other than in the south-eastward decreasing also in the western side of AH with the sharp deepening of the high density layers (Figs. 4b, 5b and 14).

As known, the volcano tectonic collapse of the Agnano caldera is delimited by two main NE–SW and NW–SE trending faults that often result from partial reactivation of pre-existent faults (Di Vito et al., 1999; De Vita et al., 1999; Smith et al., 2011; Isaia et al., 2015, 2022), our inferred lateral geological depressions, below the AH, occur in the proximity of three of these faults (a,b and c in Fig. 15 after Isaia et al., 2015) and correspond closely, or are in the immediate vicinity, of groundwater exhibiting high temperatures and TDS values.

This is evident (water samples 13, 8 and 15, in Fig. 15) for the sharp western and far eastern depressions below AH (gravimetric anomalies I and III in Figs. 4a, 5a and 15). Furthermore, piezometric outcropping occurs (water sample 14, Fig. 15) also in correspondence of both observed anomalies II and fault b (Isaia et al., 2015) (Fig. 15), probably as the fault makes the local pyroclastic materials more easily erodible. Moreover, the two depressions (anomalies I and II) show different degrees of dislocation from west to east along the northern and southern AH sides (Fig. 14). This is probably due to the fact that the main western depression of the AH (Anomalies I) also involves a NW-SE oriented structure that crosses the AH from north to south (as evidenced by the 150 m shift of anomaly I from profile north to south, Figs. 4a and 5a), this structure, conjugated with the known NE-SW fault (a in Fig. 15, Isaia et al., 2015), probably causes the greatest degree of dislocation of the western depression of AH (Fig. 14). The pronounced dislocation and fracturing within the western sector may account for the rising of thermal waters with elevated thermal levels and CO_2 content (water samples 13 and 8, set C in Section 4.4). Additionally, these geological phenomena likely contribute to the increased circulation of deep thermal fluids evidenced by the ERT analysis (Figs. 4c and 5c). So far, the presence of a large amount of mineralized water, which are not enriched by seawater input, and the understanding of the mineralization patterns in this structural controlled area, allows us to identify the best location for a geothermal exploration well, useful to derive an hydrogeological model of the area, for further low enthalpy geothermal sustainability exploitation (i.e. Corniello et al., 2015, Iorio et al., 2020). Finally, the NE-SW oriented alignment of the water samples (water samples 5, 6, 7, 2 and 15 in Fig. 15) could represent a further evidence of the extension in the subsoil of the NE-SW ring fault which delimits the south-eastern Agnano caldera rim (c in Fig. 15 Isaia et al., 2015). The NE-SW fault extension intersect the E-W caldera rim fault (d in Fig. 15 Isaia et al., 2015) probably creating an area of intense and deep fracturing which would allow the gases, feeding the spring De Pisis, to rise up.

6. Conclusions

A detailed reconstruction of the main geophysical, and geological-structural properties of a sector of Agnano caldera have been obtained by means of gravimetric, geoelectric and geochemical data acquired as part of the GeoGrid project. A three-dimensional representation of all

interpreted data sets was provided thanks to the use of the Geogrid Viewer software, which, using the developed geophysical models and integrating them with additional information from well surveys, made it possible to interpret the three-dimensional geometry and development of the main lithological interfaces of the subsurface. Therefore, it was found that the eastern sector of Agnano Caldera is characterized by a morphology strongly controlled by structural elements, which determine an uplift in the central part below the Hippodrome, and two pronounced lateral depressions. Moreover, the observed general deepening of density interface southward and southeastward, is in good agreement with the seismic bedrock trend detected by a passive seismic survey, which extends to the central part of the caldera down to −70 m, and with the presence of lava deposits found further south at −93 m. The influence of structural elements on thermal fluid circulation was also analyzed by means of density contrast and coincident resistivity changes, and it was found that both geoelectric profiles show a major circulation of deep fluid in the area coincident with the major lateral north-western depression of AH. The fluid characteristic of this area shows (except for the de Pisis spring), among the analyzed water samples, the highest temperature (39 °C), conductivity (4129 μS/cm) and hydrogen carbonate (2035 mg/L) values, and is only slightly enriched by sea water contribution. These results allow us to indicate this sector as a suitable area for future geothermal exploitation. The geochemical data extended to the entire basin confirm the structural control on the rising of gases and fluids from the depths. As a matter of fact, water samples having temperature, conductivity and hydrogen carbonate values major of 25.5 °C, 2000 μS/cm, 600 mg/L, are aligned along a NE-SW trajectory probably determined by the subsoil continuity of an outcropping fault, which was previously only hypothesized by other authors. The convergence of this fault extension with the known E-W South Agnano caldera rim fault could give rise to the De Pisis spring ($T > 57$ °C). Further analyses are certainly necessary to better understand the structural and thermal settings of the Agnano caldera and to further extend its interpretation at larger scale. The integration of additional geophysical and stratigraphic data can be particularly useful to determine lateral continuity of the inferred geological structures. This study clearly demonstrates that a multidisciplinary approach is fundamental for investigating such complex geological and geothermal areas, where several different subsurface parameters can strongly vary event at short scale. Finally, knowledge of the thermal and chemical characteristics of the Agnano caldera groundwater will allow us to identify the most suitable techniques and areas for future sustainable exploitation of geothermal resources.

CRediT authorship contribution statement

Marina Iorio: Writing – review & editing, Writing – original draft, Visualization, Supervision, Software, Methodology, Investigation, Data curation, Conceptualization. **Michele Punzo:** Writing – review & editing, Methodology, Investigation, Conceptualization. **Alberto Carotenuto:** Writing – review & editing, Supervision, Project administration, Funding acquisition. **Giuseppe Cavuoto:** Writing – review & editing, Methodology, Investigation, Conceptualization. **Alfonso Corniello:** Writing – review & editing, Methodology, Investigation, Conceptualization. **Vincenzo Di Fiore:** Writing – review & editing, Methodology, Investigation, Conceptualization. **Giampaolo Donnarumma:** Writing – review & editing, Visualization, Software, Data curation. **Maurizio Fedi:** Writing – review & editing, Methodology, Investigation, Conceptualization. **Nicola Massarotti:** Writing – review & editing, Supervision, Project administration, Funding acquisition. **Nicola Pelosi:** Writing – review & editing, Methodology, Investigation, Conceptualization. **Daniela Tarallo:** Writing – review & editing, Methodology, Investigation, Conceptualization. **Maurizio Milano:** Writing – review & editing, Methodology, Investigation, Conceptualization.

Declaration of competing interest

The authors declare that they have no known competing financial interests or personal relationships that could have appeared to influence the work reported in this paper

Data availability

The authors do not have permission to share data.

Acknowledgments

This research is financially supported by the GeoGrid project (Technologies and Innovative system for sustainability use of geothermal energy, POR Campania FESR 2014–2020). The authors would like to express their gratitude to the Agnano Hyppodrome Society for the permission to allow all geophysical and hydrochemical surveys.

Supplementary materials

Supplementary material associated with this article can be found, in the online version, at doi:10.1016/j.geothermics.2024.103049.

References

Acocella, V., 2010. Evaluating fracture patterns within a resurgent caldera: Campi Flegrei, Italy. Bull. Volcanol. 72 (5), 623–638. https://doi.org/10.1007/s00445-010-0347-x.

Adel, K., Faten, T., Belgac¸em, A., Chafai, A., Salem, B., 2012. Hydrochemical and statistical studies of the groundwater salinization in Mediterranean arid zones: case of the Jerba coastal aquifer in southeast Tunisia. Environ. Earth. Sci. 67, 2089–2100. https://doi.org/10.1007/s12665-012-1648-5.

Ahumada, M.F., Guevara, L., Favetto, A., Filipovich, R., Chiodi, A., Viramonte, J.G., Giordano, G., 2022. Electrical resistivity structure in the Tocomar geothermal system obtained from 3-D inversion of audio-magnetotelluric data (Central Puna, NW Argentina). Geothermics 104, 102436. https://doi.org/10.1016/j.geothermics.2022.102436. ISSN 0375-6505.

Albert, P.G., Giaccio, B., Isaia, R., Costa, A., Niespolo, E.M., Nomade, S., Pereira, A., Renne, P.R., Hinchliffe, A., Mark, D.F., Brown, R.J., Smith, V.C., 2019. Evidence for a large-magnitude eruption from Campi Flegrei caldera (Italy) at 29 ka. Geology 47 (7), 595–599.

Ascione, A., Aucelli, P.P.C., Cinque, A., Di Paola, G., Mattei, G., Ruello, M., Russo Ermolli, E., Santangelo, N., Valente, E., 2021. Geomorphology of Naples and the Campi Flegrei: human and natural landscapes in a restless land. J. Maps. 17 (4), 18–28. https://doi.org/10.1080/17445647.2020.1768448.

Atef, H., Abd El-Gawad, A.M.S., Abdel Zaher, M., Farag, K.S.I., 2016. The contribution of gravity method in geothermal exploration of southern part of the Gulf of Suez-Sinai region, Egypt. NRIAG J. Astron. Geophys. 5 (1), 173–185. https://doi.org/10.1016/j.nrjag.2016.02.005.

Autorità di Bacino Nord-Occidentale della Campania, 2004. Piano di Tutela delle Acque. Il contributo al Piano di Tutela delle Acque della Regione Campania. 3 Vol. SELCA Ed.

Baniamerian, J., Fedi, M., Oskooi, B., 2016. Research note: compact depth from extreme points: a tool for fast potential field imaging. Geophys. Prospect. 64 (5), 1386–1398.

Barone, A., Fedi, M., Tizzani, P., Castaldo, R., 2019. Multiscale Analysis of DInSAR Measurements for Multi-Source Investigation at Uturuncu Volcano (Bolivia). Remote Sens. (Basel) 11, 703. https://doi.org/10.3390/rs11060703.

Bevilacqua, A., Flandoli, F., Neri, A., Isaia, R., Vitale, S., 2016. Temporal models for the episodic volcanism of Campi Flegrei caldera (Italy) with uncertainty quantification. J. Geophys. Res. Solid Earth 121, 7821–7845. https://doi.org/10.1002/2016JB013171.

Bruno, P.P.G., Ricciardi, G.P., Petrillo, Z., Di Fiore, V., Troiano, A., Chiodini, G., 2007. Geophysical and hydrogeological experiments from a shallow hydrothermal system at Solfatara Volcano, Campi Flegrei, Italy: response to caldera unrest. J. Geophys. Res. 112 (B06201) https://doi.org/10.1029/2006JB004383.

Buono, G., Paonita, A., Pappalardo, L., Caliro, S., Tramelli, A., Chiodini, G., 2022. New insights into the recent magma dynamics under Campi Flegrei Caldera (Italy) from petrological and geochemical evidence. J. Geophys. Res. 127 (3).

Byrdina, S., Vandemeulebrouck, J., Cardellini, C., Legaz, A., Camerlynck, C., Chiodini, G., Caliro, S., 2014. Relations between electrical resistivity, carbon dioxide flux, and self-potential in the shallow hydrothermal system of Solfatara (Phlegrean Fields, Italy). J. Volcanol. Geotherm. Res. 283, 172–182. https://doi.org/10.1016/j.jvolgeores.2014.07.010.

Blázquez, C.S., Ignacio, M.N., Maté González, M.A., García, P.C., Martín, A.F., González-Aguilera, D., 2022. Geophysical exploration for shallow geothermal applications: a case study in Artà, (Balearic Islands, Spain). Geothermics 105, 102517. https://doi.org/10.1016/j.geothermics.2022.102517. ISSN 0375-6505.

Calise, F., Di Fraia, S., Macaluso, A., Massarotti, N., Vanoli, L., 2018. A geothermal energy system for wastewater sludge drying and electricity production in a small island. Energy 163, 130–143.
Cardellini, C., Chiodini, G., Frondini, F., Avino, R., Bagnato, E., Caliro, S., Lelli, M., Rosiello, A., 2017. Monitoring diffuse volcanic degassing during volcanic unrests: the case of Campi Flegrei (Italy). Sci. Rep. 7 (1), 6757. https://doi.org/10.1038/s41598-017-06941-2.
Carlino, S., Somma, R., Troise, C., De Natale, G., 2012. The geothermal exploration of Campanian volcanoes: historical review and future development. Renew. Sustain. Energy Rev. 16 (1), 1004–1030. https://doi.org/10.1016/j.rser.2011.09.023.
Carlino, S., Troiano, A., Di Giuseppe, M.G., Tramelli, A., Troise, C., Somma, R., De Natale, G., 2016. Exploitation of geothermal energy in active volcanic areas: a numerical modelling applied to high temperature Mofete geothermal field, at Campi Flegrei caldera (Southern Italy). Renew. Energy 87 (1), 54–66. https://doi.org/10.1016/j.renene.2015.10.007.
Carotenuto, A., De Luca, G., Fabozzi, S., Figaj, R.D., Iorio, M., Massarotti, N., Vanoli, L., 2016. Energy analysis of a small geothermal district heating system in southern Italy. Int. J. Heat Technol. 34 (2), S519–S527.
Carrier, A., Fischanger, F., Gance, J., Cocchiararo, G., Morelli, G., Lupi, M., 2019. Deep electrical resistivity tomography for the prospection of low- to medium-enthalpy geothermal resources. Geophys. J. Int. 219 (3), 2056–2072. https://doi.org/10.1093/gji/ggz411.
Castaldo, R., D'Auria, L., Pepe, S., Solaro, G., De Novellis, V., Tizzani, P., 2019. The impact of crustal rheology on natural seismicity: Campi Flegrei caldera case study. Geosci. Front. 10, 453–466. https://doi.org/10.1016/j.gsf.2018.02.003.
Charlton, D., Kilburn, C., Edwards, S., 2020. Volcanic unrest scenarios and impact assessment at Campi Flegrei caldera, Southern Italy. J. Appl. Volcanol. 9 (1), 1–26.
Chiodini, G., Frondini, C., Cardellini Granieri, D., Marini, L., Ventura, G., 2001. CO_2 degassing and energy release at Solfatara volcano, Campi Flegrei, Italy. J. Geophys. Res. 106 (B8), 16.213–16.221.
Chiodini, G., Vandemeulebrouck, J., Caliro, S., D'Auria, L., De Martino, P., Mangiacapra, A., Petrillo, Z., 2015. Evidence of thermal driven processes triggering the 2005–2014 unrest at Campi Flegrei caldera. Earth Planet. Sci. Lett. 414, 58–67. https://doi.org/10.1016/j.epsl.2015.01.012.
Chiodini, G., Paonita, A., Aiuppa, A., Costa, A., Caliro, S., De Martino, P., Acocella, V., Vandemeulebrouck, J., 2016. Magmas near the critical degassing pressure drive volcanic unrest towards a critical state. Nat. Commun. 7 (1), 13712. https://doi.org/10.1038/ncomms13712.
Corniello, A., Nicotera, P., 1981. Geologia, Idrogeologia e Idro-Chimica Della Zona Sud-Occidentale Dei Campi Flegrei. Memorie e Note Istituto di Geologia Applicata, Napoli, p. 16.
Corniello, A., 2009. Considerations on the hydrochemical characteristics of groundwater in the Phlegrean and Vesuvian areas (in Italian). In: Calcaterra, D., Morra, V. (Eds.), Volume Mountains of fire: Risks and Resources in Volcanic Areas of Vesuvius and Etna, 978-88-6026-118-2. Luciano Editore, Napoli, pp. 125–138.
Corniello, A., Cardellicchio, N., Cavuoto, G., Cuoco, E., Ducci, D., Minissale, A., Mussi, M., Petruccione, E., Pelosi, N., Rizzo, E., Polemio, M., Tamburino, S., Tedesco, D., Tiano, P., Iorio, M., 2015. Hydrogeological characterization of a geothermal system: the case of the thermo-mineral area of Mondragone (Campania, Italy). Int. J. Environ. Res. 9, 523–534.
Corrado, G., De Lorenzo, S., Monelli, F., Tramacere, A., Zito, G., 1998. Surface heat flow density at the Phlegrean fields caldera (Southern Italy). Geothermics. 27 (4), 469–484.
Costa, A., Folch, A., Macedonio, G., Giaccio, B., Isaia, R., Smith, V.C., 2012. Quantifying volcanic ash dispersal and impact of the Campanian ignimbrite super-eruption. Geophys. Res. Lett. 39 (10).
D'Auria, L., Giudicepietro, F., Aquino, I., Borriello, G., Del Gaudio, C., Lo Bascio, D., Martini, M., Ricciardi, G.P., Ricciolino, P., Ricco, C., 2011. Repeated fluid-transfer episodes as a mechanism for the recent dynamics of Campi Flegrei caldera (1989–2010). J. Geophys. Res. 116, B04313. https://doi.org/10.1029/2010JB007837.
De Giorgi, L., Leucci, G., 2015. Study of shallow low-enthalpy geothermal resources using integrated geophysical methods. Acta Geophys 63, 125–153. https://doi.org/10.2478/s11600-014-0243-4.
Deino, A.L., Orsi, G., de Vita, S., Piochi, M., 2004. The age of the Neapolitan yellow tuff caldera-forming eruption (Campi Flegrei caldera -Italy) assessed by 40Ar/39Ar dating method. J. Volcanol. Geotherm. Res. 133, 157–170. https://doi.org/10.1016/S0377-0273(03)00396-2.
Delaunay, B., 1934. Sur la sphère vide. A la mémoire de Georges Voronoi. Izv. Akad. Nauk SSSR, Otdelenie Matematicheskih i Estestvennyh Nauk 7, 793800.
Delgado, J., Lopez Casado, C., Giner, J., Estevez, A., Cuenca, A., Molina, S., 2000. Microtremors as a geophysical exploration tool: applications and limitations. Pure Appl. Geophys. 157, 1445–1462.
De Vita, S., Orsi, G., Civetta, L., Carandente, A., D'Antonio, M., Deino, A., Di Cesare, T., Di Vito, M., Fisher, R.V., Isaia, R., Marotta, E., Necco, A., Ort, M., Pappalardo, L., Piochi, M.A., Southon, J., 1999. The Agnano monte spina eruption (4100 years BP) in the restless Campi Flegrei caldera (Italy). J. Volcanol. Geotherm. Res. 91 (2–4), 269–301.
De Vita, P., Allocca, V., Celico, F., Fabbrocino, S., Mattia, C., Monacelli, G., Musilli, I., Piscopo, V., Scalise, A.R., Summa, G., Tranfaglia, G., Celico, P., 2018. Hydrogeology of continental southern Italy. J. Maps 14 (2), 230–241.
Di Fiore, V., Punzo, M., Cavuoto, G., Galli, P., Mazzola, S., Pelosi, N., Tarallo, D., 2020. Geophysical approach to study the potential ocean waveinduced liquefaction: an example at Magoodhoo Island (Faafu Atoll, Maldives, Indian Ocean). Mar. Geophys. Res. 41, 9. https://doi.org/10.1007/s11001-020-09408-8.
Di Fraia, S., Macaluso, A., Massarotti, N., Vanoli, L., 2019. Energy, exergy and economic analysis of a novel geothermal energy system for wastewater and sludge treatment. Energy Convers. Manag. 195, 533–547. https://doi.org/10.1016/j.enconman.2019.05.035.
Di Giuseppe, M.G., Troiano, A., 2019. Monitoring active fumaroles through time-lapse electrical resistivity tomograms: an application to the Pisciarelli fumarolic field (Campi Flegrei, Italy). J. Volcanol. Geotherm. Res. 375, 32–42. https://doi.org/10.1016/j.jvolgeores.2019.03.009.
Di Stefano, P., Luzio, D., Renda, P., Martorana, R., Capizzi, P., D'Alessandro, A., Messina, N., Napoli, G., Todaro, S., Zarcone, G., 2014. Integration of HVSR measures and stratigraphic constraints for seismic microzonation studies: the case of Oliveri (ME). Nat. Hazards Earth Syst. Sci. Discuss. 2, 2597–2637. https://doi.org/10.5194/nhessd-2-2597-2014.
Di Vito, M.A., Isaia, R., Orsi, G., Southon, J., De Vita, S., D'Antonio, M., Pappalardo, L., Piochi, M, 1999. Volcanism and deformation since 12,000 years at the Campi Flegrei caldera (Italy). J. Volcanol. Geotherm. Res. 91 (2–4), 221–246.
Drahor, M.G., Berge, M.A., Bakak, Ö., Öztürk, C., 2014. Electrical resistivity tomography monitoring studies at Balçova (Turkey) geothermal site. Near. Surf. Geophys. 12, 337–350.
Ebrahimi, P., Guarino, A., Allocca, V., Caliro, S., Avino, R., Bagnato, E., Capecchiacci, F., Carandente, A., Minopoli, C., Santi, A., Albanese, S., 2022. Hierarchical clustering and compositional data analysis for interpreting groundwater hydrogeochemistry: the application to Campi Flegrei volcanic aquifer (south Italy). J. Geochem. Explor. 233, 106922 https://doi.org/10.1016/j.gexplo.2021.106922.
Fedi, M., 2006. DEXP: a fast method to determine the depth and the structural index of potential fields sources. Geophysics 72 (1), I1–I11.
Fedi, M., Florio, G., Quarta, T., 2007. Multiridge analysis and reduced Euler deconvolution, in: SEG technical program expanded abstracts 2007. In: Presented at the SEG Technical Program Expanded Abstracts 2007. Society of Exploration Geophysicists, pp. 780–784. https://doi.org/10.1190/1.2792528.
Fedi, M., Florio, G., Quarta, T., 2009. Multiridge analysis of potential fields: geometric method and reduced Euler deconvolution. Geophysics 74, L53–L65. https://doi.org/10.1190/1.3142722.
Fedi, Pilkington, 2012. Understanding imaging methods for potential field data. Geophysics 77 (1), G13–G24. https://doi.org/10.1190/geo2011-0078.1.
Florio, G., Fedi, M., 2006. Euler deconvolution of vertical profiles of potential field data. In: SEG Technical Program Expanded Abstracts 2006. Society of Exploration Geophysicists, pp. 958–962.
Gebauer, S.K., Schmitt, A.K., Pappalardo, L., Stockli, D.F., Lovera, O.M., 2014. Crystallization and eruption ages of Breccia Museo (Campi Flegrei caldera, Italy) plutonic clasts and their relation to the Campanian ignimbrite. Contributions to Mineralogy and Petrology 167, 1–18. https://doi.org/10.1007/s00410-013-0953-7.
Giaccio, B., Isaia, R., Fedele, F.G., Di Canzio, E., Hoffecker, J., Ronchitelli, A., Sinitsyn, A. A., Anikovich, M., Lisitsyn, S.N., Popov, V.V., 2008. The campanian ignimbrite and codola tephra layers: two temporal/stratigraphic markers for the early upper palaeolithic in southern Italy and Eastern Europe. J. Volcanol. Geoth. Res. 177 (1), 208–226.
Giaccio, B., Hajdas, I., Isaia, R., Deino, A., Nomade, S., 2017. High-precision 14C and 40 Ar/39 Ar dating of the Campanian Ignimbrite (Y-5) reconciles the time-scales of climatic-cultural processes at 40 ka. Sci. Rep. 7 (1), 1–10.
Gola, G., Barone, A., Castaldo, R., Chiodini, G., D'Auria, L., García-Hernández, R., Pepe, S., Solaro, G., Tizzani, P., 2021. A novel multidisciplinary approach for the Thermo-rheological study of volcanic areas: the case study of Long Valley caldera. J. Geophys. Res. Solid Earth 126. https://doi.org/10.1029/2020jb020331.
Gómez-Ortiz, D., Martín-Velázquez, S., Martín-Crespo, T., Márquez, A., Lillo, J., López, I., Carreño, F., Martín-González, F., Herrera, R., De Pablo, M.A., 2007. Joint application of ground penetrating radar and electrical resistivity imaging to investigate volcanic materials and structures in Tenerife (Canary Islands, Spain). J. Appl. Geophys. 62 (3), 287–300. https://doi.org/10.1016/j.jappgeo.2007.01.002. ISSN 0926-9851.
Gresse, M., Vandemeulebrouck, J., Byrdina, S., Chiodini, G., Revil, A., Johnson, T.C., Ricci, T., Vilardo, G., Mangiacapra, A., Lebourg, T., Grangeon, J., Bascou, P., Metral, L., 2017. Three-dimensional electrical resistivity tomography of the Solfatara Crater (Italy): implication for the multiphase flow structure of the shallow hydrothermal system. J. Geophys. Res. Solid Earth 122, 8749–8768. https://doi.org/10.1002/2017JB014389.
Guglielmetti, L., Moscariello, A., 2021. On the use of gravity data in delineating geologic features of interest for geothermal exploration in the Geneva Basin (Switzerland): prospects and limitations. Swiss. J. Geosci. 114, 15. https://doi.org/10.1186/s00015-021-00392-8.
Ibs-von Seht, M., Wohlenberg, J., 1999. Microtremor measurements used to map thickness of soft sediments. Bull. Seismol. Soc. Am. 89, 250–259.
Imposa, S., Panzera, F., Grassi, S., Lombardo, G., Catalano, S., Romagnoli, G., Tortorici, G., 2017. Geophysical and geologic surveys of the areas struck by the August 26th 2016 Central Italy earthquake: the study case of Pretare and Piedilama. J. Appl. Geophy. 145, 17–27. https://doi.org/10.1016/j.jappgeo.2017.07.016.
Ingebritsen, S., Sanford, W., Neuzil, C., 2008. Groundwater in Geologic Processes, 2nd edition, Cambridge.
Iorio, M., Carotenuto, A., Corniello, A., Di Fraia, S., Massarotti, N., Mauro, A., Somma, R., Vanoli, L., 2020. Low enthalpy geothermal system in structural controlled areas: a suistainability analysis of geothermal resources for heating Plant (The Mondragone case in Southern Appennines, Italy). Energies (Basel) 13 (5), 1237. https://doi.org/10.3390/en13051237.
Isaia, R., Di Giuseppe, M.G., Troiano, A., Avino, R., Caliro, S., Santi, A., Vitale, S., 2022. Structure and present state of the Astroni Volcano in the Campi Flegrei caldera in Italy based on multidisciplinary investigations. Geochem. Geophys. Geosyst. 23, e2022GC010534 https://doi.org/10.1029/2022GC010534.

Isaia, R., Vitale, S., Di Giuseppe, M.G., Iannuzzi, E., D'Assisi Tramparulo, F., Troiano, A., 2015. Stratigraphy, structure, and volcano-tectonicevolution of Solfatara maar-diatreme (Campi Flegrei, Italy). Geol. Soc. Am. Bull. 127 (9–10), 1485–1504. https://doi.org/10.1130/B31183.1.

Isaia, R., D'Antonio, M., Dell'Erba, F., Di Vito, M.A., Orsi, G., 2004. The Astroni volcano: the only example of closely spaced eruptions in the same vent area during the recent history of Campi Flegrei caldera (Italy). J. Volcanol. Geotherm. Res. 133, 171–192.

Kelemework, Y., Milano, M., La Manna, M., de Alteriis, G., Iorio, M., Fedi, M., 2021. Crustal structure in the Campanian region (Southern Apennines, Italy) from potential field modelling. Sci. Rep. 11 (1), 14510. https://doi.org/10.1038/s41598-021-93945-8.

Komori, S., Utsugi, M., Kagiyama, T., Inoue, H., Chen, C.-H., Chiang, H.-T., Fong Chao, B., Yoshimura, R., Kanda, W., 2014. Hydrothermal system in the Tatun Volcano Group, northern Taiwan, inferred from crustal resistivity structure by audio-magnetotellurics. Prog. in Earth Planet. Sci. 1, 20. https://doi.org/10.1186/s40645-014-0020-7.

Konno, K., Ohmachi, T., 1998. Ground-motion characteristics estimated from spectral ratio between horizontal and vertical components of microtremor. Bull. Seismol. Soc. Am. 88 (1), 228–241.

Kramer, S.L., 1996. Geotechnical Earthquake Engineering. Prentice Hall Inc, New Jersey, p. 653.

La Brecque, D.J., Miletto, M., Daily, W., Ramirez, A., Owen, E., 1996. The effects of noise on Occam's inversion of resistivity tomography data. Geophysics 61, 538–548.

Leone, U., D'Antonio, M., Orsi, G, 2022. The Urban Development of Campi Flegrei, Italy. In: Orsi, G., D'Antonio, M., Civetta, L. (Eds.), Campi Flegrei. Active Volcanoes of the World. Springer, Berlin, Heidelberg. https://doi.org/10.1007/978-3-642-37060-1_15.

Lichoro, C.M., Árnason, K., Cumming, W., 2019. Joint interpretation of gravity and resistivity data from the Northern Kenya volcanic rift zone: structural and geothermal significance. Geothermics 77, 139–150. https://doi.org/10.1016/j.geothermics.2018.09.006. ISSN 0375-6505.

Liu, S., Baniamerian, J., Fedi, M., 2020. Imaging methods versus inverse methods: an option or an alternative? IEEE Transact. Geosci. Remote Sens. 58 (5), 3484–3494.

Loke, M.H., Barker, R.D., 1996a. Rapid least-squares inversion of apparent resistivity Pseudosections by a quasi-newton method. Geophys. Prospect. 44, 131–152. https://doi.org/10.1111/j.1365-2478.1996.tb00142.x.

Loke, M.H., Barker, R.D., 1996b. Practical techniques for 3D resistivity surveys and data inversion. Geophys. Prospect. 44 (3), 499–523. https://doi.org/10.1111/j.1365-2478.1996.tb00162.x.

Mastellone, D., Fedi, M., Ialongo, S., Paoletti, V., 2014. Volume continuation of potential fields from the minimum-length solution: an optimal tool for continuation through general surfaces. J. Appl. Geophys. 111, 346–355.

Milsom, J., Eriksen, A., 2011. Field Geophysics, 4th review edition. Wiley Publishers, Chichester, p. 304.

Milano, M., Kelemework, Y., La Manna, M., Fedi, M., Montanari, D., Iorio, M., 2020. Crustal structure of Sicily from modelling of gravity and magnetic anomalies. Sci. Rep. 10, 16019. https://doi.org/10.1038/s41598-020-72849-z.

Milano, M., Varfinezhad, R., Bizhani, H., Moghadasi, M., Kalateh, A.N., Baghzendani, H., 2021. Joint interpretation of magnetic and gravity data at the Golgohar mine in Iran. J. Appl. Geophys. 195, 104476 https://doi.org/10.1016/j.jappgeo.2021.104476.

Mitjanas, G., Ledo, J., Macau, A., Alías, G., Queralt, P., Bellmunt, F., Rivero, Ll., Gabàs, A., Marcuello, A., Benjumea, B., Martí, A., Figueras, S., 2021. Integrated seismic ambient noise, magnetotellurics and gravity data for the 2D interpretation of the Vallès basin structure in the geothermal system of La Garriga-Samalús (NE Spain). Geothermics 93, 102067. https://doi.org/10.1016/j.geothermics.2021.102067. ISSN 0375-6505.

Molnar, S., Sirohey, A., Assaf, J., et al., 2022. A review of the microtremor horizontal-to-vertical spectral ratio (MHVSR) method. J. Seismol. 26, 653–685. https://doi.org/10.1007/s10950-021-10062-9.

Mulargia, F., Castellaro, S., 2016. HVSR deep mapping tested down to 1.8 km in Po Plane Valley, Italy. Phys. Earth Planet Interiors 61 (Part A), 17–23.

Muth, C.J., Aalto, P., Mylläri, F., Rönkkö, T., Harsia, P., 2021. Chapter 2 - Globally and locally applicable technologies to accelerate electrification. In: Pami, P. (Ed.), Electrification. Academic Press, pp. 25–55. https://doi.org/10.1016/B978-0-12-822143-3.00005-6. ISBN 9780128221433.

Nakamura, Y., 1989. A method for dynamic characteristics estimation of subsurface using microtremor on the ground surface. Quarter. Rep. RTRI Railway Tech. Res. Institute (RTRI) 30 (1), 25–30.

Nardone, L., Esposito, R., Galluzzo, D., Petrosino, S., Cusano, P., La Rocca, M., Di Vito, M. A., Bianco, F., 2020. Array and spectral ratio techniques applied to seismic noise to investigate the Campi Flegrei (Italy) subsoil structure at different scales. Adv. Geosci. 52, 75–85. https://doi.org/10.5194/adgeo-52-75-2020.

Orsi, G., D'Antonio, M., de Vita, S., Gallo, G., 1992. The Neapolitan Yellow Tuff, a large-magnitude trachytic Phreatoplinian eruption: eruptive dynamics, magma withdrawal and caldera collapse. J. Volcanol. Geoth. Res. 53 (1–4), 275–287.

Orsi, G., De Vita, S., Di Vito, M.A., 1996. The restless, resurgent Campi Flegrei nested caldera (Italy): constraints on its evolution and configuration. J. Volcanol. Geoth. Res. 74 (3–4), 179–214.

Orsi, G., Di Vito, M.A., Isaia, R., 2004. Volcanic hazard assessment at the restless Campi Flegrei caldera. Bull. Volcanol. 66, 514–530.

Orsi, G., 2022. Volcanic and Deformation History of the Campi Flegrei Volcanic Field, Italy. In: Orsi, G., D'Antonio, M., Civetta, L. (Eds.), Campi Flegrei. Active Volcanoes of the World. Springer, Berlin, Heidelberg. https://doi.org/10.1007/978-3-642-37060-1_1.

Paoletti, V., Milano, M., Baniamerian, J., Fedi, M., 2020. Magnetic field imaging of salt structures at Nordkapp Basin, Barents Sea. Geophys. Res. Lett. https://doi.org/10.1029/2020GL089026.

Paoletti, V., Hintersberger, E., Schattauer, I., Milano, M., Deidda, G.P., Supper, R., 2022. Geophysical study of the Diendorf-Boskovice fault system (Austria). Remote Sens. (Basel) 14, 1807. https://doi.org/10.3390/rs14081807.

Parolai, S., Bormann, P., Milkereit, C., 2002. New relationships between Vs, thickness of sediments and resonance frequency calculated from H/V ratio of seismic noise for the Cologne area. Bull. Seism. Soc. Am. 92, 2521–2527.

Pepe, S., De Siena, L., Barone, A., Castaldo, R., D'Auria, L., Manzo, M., Casu, F., Fedi, M., Lanari, R., Bianco, F., Tizzani, P., 2019. Volcanic structures investigation through SAR and seismic interferometric methods: the 2011–2013 Campi Flegrei unrest episode. Remote Sens. Environ. 234, 111440 https://doi.org/10.1016/j.rse.2019.111440.

Petrosino, P., Cusano, P., Saccarotti, G., 2006. Shallow shear-wave velocity structure of Solfatara volcano (Campi Flegrei, Italy), from inversion of Rayleigh-wave dispersion curves. Bollettino di Geofisica Teorica ed Applicata 47 (1–2), 89–103. March-June.

Reid, A.B., Allsop, J.M., Granser, H., Millett, A.J., Somerton, I.W., 1990. Magnetic interpretation in three dimensions using Euler deconvolution. Geophysics 55, 80–91. https://doi.org/10.1190/1.1442774.

Rosi, M., Sbrana, A., 1987. Phlegrean fields. CNR Quaderni de "La Ricerca Scientifica". Roma 114 (9), 1–175.

Sakhare, V., Kant, A., Low, U., Biswal, B.P., Paul, S., Hanmanthu, D., 2023. Gravity and magneto-telluric study of Manuguru geothermal field, Telangana state, India. Geothermics 109, 102650. https://doi.org/10.1016/j.geothermics.2023.102650. ISSN 0375-6505.

Sasaki, Y., 1992. Resolution of resistivity tomography inferred from numerical simulation. Geophys. Prospect. 40, 453–464.

Scarpati, C., Cole, P., Perrotta, A., 1993. The Neapolitan Yellow Tuff—A large volume multiphase eruption from Campi Flegrei, southern Italy. Bull. Volcanol. 55 (5), 343–356.

Scarpati, C., Perrotta, A., Lepore, S., Calvert, A., 2013. Eruptive history of Neapolitan volcanoes: constraints from 40Ar–39Ar dating. Geol. Mag. 150 (3), 412–425.

Scarpati, C., Sparice, D., Perrotta, A., 2020. Dynamics of large pyroclastic currents inferred by the internal architecture of the Campanian Ignimbrite. Sci. Rep. 10 (1), 1–13.

Sepede, G., Alimonti, C., Gómez-Lopera, S.Á., Ataieyan, A., 2022. Numerical evaluation of thermal and hydrodynamic effects caused by heat production well on geothermal Phlegraean Fields. Front. Energy Res. 10, 1000990 https://doi.org/10.3389/fenrg.2022.1000990.

SESAME, 2004. Guidelines for the implementation of the H/V spectral ratio technique on ambient vibrations: measurements, processing and interpretation. SESAME European research project WP12, deliverable D23.12 (http://sesame-fp5.obs.ujf-grenoble.fr/Deliverables 2004).

Silleni, A., Giordano, G., Isaia, R., Ort, M.H., 2020. The Magnitude of the 39.8 Ka Campanian ignimbrite Eruption, Italy: method, uncertainties and errors. Field data, models and uncertainty in hazard assessment of pyroclastic density currents and lahars: global perspectives. Simpkin, P.G., Davis, A., 1993.

Siniscalchi, A., Tripaldi, S., Romano, G., Chiodini, G., Improta, L., Petrillo, Z., D'Auria, L., Caliro, S., Avino, R., 2019. Reservoir structure and hydraulic properties of the Campi Flegrei geothermal system inferred by audiomagnetotelluric, geochemical, and seismicity study. J. Geophys. Res. Solid Earth 124, 5336–5356. https://doi.org/10.1029/2018JB016514.

Smith, V.C., Isaia, R., Pearce, N.J.G., 2011. Tephrostratigraphy and glass compositions of post-15 ka Campi Flegrei eruptions: implications for eruption history and chronostratigraphic markers. Quat. Sci. Rev. 30 (25), 3638–3660.

Telford, W.M., Geldart, L.P., Sheriff, R.E., 1990. Resistivity methods. Applied Geophysics, 2nd Edition. Cambridge Univ. Press, Cambridge, UK, pp. 353–358. https://doi.org/10.1017/cbo9781139167932.012.

Tonarini, S., D'Antonio, M., Di Vito, M.A., Orsi, G., Carandente, A., 2009. Geochemical and B-Sr-Nd isotopic evidence for mingling and mixing processes in the magmatic system feeding the Astroni volcano (4.1-3.8ka) within the Campi Flegrei caldera (South Italy). Lithos 107, 135–151.

Tramelli, A., Del Pezzo, E., Bianco, F., Boschi, E., 2006. 3D scattering image of the Campi Flegrei caldera (Southern Italy): new hints on the position of the old caldera rim. Phys. Earth Planet. Interiors 155 (3–4), 269–280. https://doi.org/10.1016/j.pepi.2005.12.009.

Tramelli, A., Godano, C., Ricciolino, P., Giudicepietro, F., Caliro, S., Orazi, M., De Martino, P., Chiodini, G., 2021. Statistics of seismicity to Investigate the Campi flegrei caldera unrest. Sci. Rep. 11 (1) https://doi.org/10.1038/s41598-021-86506-6.

Tramelli, A., Giudicepietro, F., Ricciolino, P., Chiodini, G., 2022. The seismicity of Campi Flegrei in the contest of an evolving long-term unrest. Sci. Rep. 12, 2009.

Troiano, A., Di Giuseppe, M.G., Isaia, R., 2022. 3D structure of the Campi Flegrei caldera central sector reconstructed through short-period magnetotelluric imaging. Sci. Rep. 12, 20802. https://doi.org/10.1038/s41598-022-24998-6.

Valentino, G.M., Stanzione, D., 2004. Geochemical monitoring of the thermal waters of Phlegraean Fields. J. Volcanol. Geotherm. Res. 133, 261–289.

Varfinezhad, R., Fedi, M., Milano, M., 2022. The role of model weighting functions in the gravity and DC resistivity inversion. IEEE Transact. Geosci. Remote Sensing A Publ. IEEE Geosci. Remote Sens. Soc. 60, 1–15. https://doi.org/10.1109/TGRS.2022.3149139.

Vaselli, O., Tassi, F., Tedesco, D., Poreda, J.R., Caprai, A., 2011. Submarine and inland gas discharges from the Campi Flegrei (southern Italy) and the Pozzuoli Bay: geochemical clues for a common hydrothermal-magmatic source. Proc. Earth Planet. Sci. 4, 57–73.

Venturi, S., Tassi, F., Bicocchi, G., Cabassi, J., Capecchiacci, F., Capasso, G., Vaselli, O., Ricci, A., Fausto Grassa, F., 2017. Fractionation processes affecting the stable carbon isotope signature of thermal waters from hydrothermal/volcanic systems: the examples of Campi Flegrei and Vulcano Island (southern Italy). J. Volcanol. Geotherm. Res. 345, 46–57.

Wathelet, M., Chatelain, J.L., Cornou, C., Di Giulio, G., Guillier, B., Ohrnberger, M., Savvaidis, A., 2020. Geopsy: a user-friendly open-source tool set for ambient vibration processing. Seismol. Res. Lett. 91, 1878–1889.

Young, N., Isaia, R., Gottsmann, J., 2020. Gravimetric constraints on the hydrothermal system of the Campi Flegrei caldera. J. Geophys. Res. Solid Earth 125 (7), e2019JB019231.

Yasong, L., Chunlei, L., Shengwei, C., Qingzhuang, M., Yan, D., Zhenjiao, J., 2021. Br/Cl ratio, Zn and radon constraints on the origin and fate of geothermal fluids in the coastal region of southeastern China. Hydrogeol. J. 29, 2211–2218. https://doi.org/10.1007/s10040-021-02373-5.

Yongje, K., Kwang-Sik, L., Dong-Chan, K., Dae-Ha, L., Seung-Gu, L., Won-Bae, P., Gi-Won, K., Nam-Chil, W., 2003. Hydrogeochemical and isotopic evidence of groundwater salinization in a coastal aquifer: a case study in Jeju volcanic island, Korea. J. Hydrol. (Amst) 270, 282–294.